Design Modifications of a UAV Wing for Optimal Integration of a Magnetic Anomaly Detection Sensor

Gonçalo Ferreira Gameiro

Thesis to obtain the Master of Science Degree in

Aerospace Engineering

Supervisors: Prof. Afzal Suleman

Examination Committee

Chairperson: Prof. Filipe Szolnoky Ramos Pinto Cunha
Supervisor: Prof. Afzal Suleman
Member of the Committee: Major Dr. Luís Filipe da Silva Félix

November 2018

To my family and friends

Acknowledgements

Although this work was only developed in the last six months, it is the culminate of everything I learnt in the last six, which were similar to a roller-coaster. There are several people that, in their own way, helped me to conclude my studies and to grow as person, to whom I would like to express my gratitude.

I would like to thank my supervisor, Prof. Afzal Suleman, for the opportunity to be part of this project at the University of Victoria Centre for Aerospace Research, in Canada, the guidance, patience and kindness during the development of this work and all the support during my stay abroad. I would also like to thank Major Luís Félix for the support and availability during the application period, allowing this adventure to be possible.

To the staff from CfAR, for the warm receptivity, support and joy. Also, for the valuable knowledge they shared, and the opportunity to be part of a flight test crew. Finally, for all the good moments during work, that made every day a little easier. I would like express my gratitude to Doctor Jenner Richards for all the initial guidance and for sharing his knowledge on the aircraft in study.

I would like to thank my friends that also travelled to Canada for their projects. To them, my deep thankfulness for all the trips, hangouts and companionship, which helped to feel little a bit like home.

To Cody Hansen, who I owe a huge thank you, for the project management and for sharing his military experience. For an ”indirect” guidance on this project and the fact we could talk about our work and debate ideas, which helped me a lot to see things from a different perspective. Your support throughout this project was extraordinary.

I also would like to express my gratitude to Brenda Sutton, who accommodate me in Victoria. I will never forget your kindness, support and knowledge, and specially the good chats at the end of the day.

To the Portuguese Air Force Academy, for teaching me the moral values that helped me grow as a person.

To my friends from Técnico, for all the good experiences, the support, motivation and hangouts. Also to my hometown friends, who always showed their kindness and friendship, despite my absence during my course.

A special thank you to my comrades, Barões, who helped and motivated me to surpass all the difficulties during my training in the Academy. For the memories and experience we have, that means a lot to me.

To my family, especially to my parents and brother, whom always supported from the first times. For the love, support and encouragement that always help me to get through my obstacles.

To Filipa, for the love and unmeasurable support, that helped me keeping motivated during my studies and journey abroad.

Abstract

This work describes the conceptual design of a Unmanned Air Vehicle (UAV) wing with a Magnetic Anomaly Detection (MAD) sensor for submarine detection operations. Nowadays, underwater marine vessels are able to evade conventional detection methods such as sonar. Therefore, it is necessary to integrate MAD sensors in modern Anti-Submarine Warfare theatres. UAVs typically generate a magnetic field due to the electrical systems on board, causing interference noise on the MAD sensor data analysis and compromising its performance. To address these issues, a characterization of the aircraft's magnetic signature was conducted, and it was found that the wing tip and a tail stinger boom are the best options to minimize the magnetic noise. A structural and aerodynamic analysis of the aircraft showed the wing tip configuration was the best option since the amount of mass required to counter the moment of a tail stinger boom would require major modifications on the UAV. Also, the aircraft magnetic signature is minimum at the wing tip, with an intensity of -2.9nT. An aerodynamic characterization of the aircraft was carried to evaluate the effect of the MAD pods on the wingtips. A parametric optimization of the wing was conducted. Given the dimensional constraints on the wing structure and a target magnetic noise of 2nT at the wing tip, the optimizer objective function was to minimize the total fuel consumption. The optimum solution allowed a decrease of 30% on the magnetic noise and a fuel consumption of 8.71 kg of fuel for an 8-hour search operation.

Keywords

Aircraft Design, Unmanned Aerial Vehicle, Anti-Submarine Warfare, Magnetic Anomaly Detection sensor, Parametric Optimization

Resumo

Este trabalho descreve o processo de projeto conceptual de uma asa de um Veículo Aéreo Não-Tripulado (VANT) com um sensor de anomalias magnéticas (AM) para ser usado em deteção de submarinos. Atualmente, estes veículos estão dotados com capacidades que diminuem as hipóteses de deteção por métodos convencionais, como o sonar. Assim, torna-se necessário integrar sensores de AM em cenários atuais de Guerra Anti-Submarina. Os sistemas aviónicos destas aeronaves geram um campo magnético que causa interferência no sensor de AM, causando ruído nos dados da análise e comprometendo a sua eficiência. Para evitar este problema, realizou-se uma caracterização da assinatura magnética da aeronave, concluindo que as pontas das asas e uma configuração de arpão na cauda seriam as melhores soluções para colocar o sensor, a fim de minimizar a interferência magnética. Estudos estruturais e aerodinâmicos revelaram que a primeira seria a melhor opção, pois a massa necessária para anular o momento gerado na segunda requeria alterações substanciais na estrutura da aeronave. A ponta da asa era também o local com menor nível de assinatura magnética. Realizou-se uma otimização paramétrica da asa da aeronave, considerando os efeitos aerodinâmicos dos invólucros do sensor. Atendendo às restrições no dimensionamento da estrutura da asa e a um valor de interferência magnética, o otimizador teria como objetivo minimizar o consumo total de combustível. A solução ótima permitiu reduzir em 30% o valor da assinatura magnética na ponta da asa e obter uma configuração que, numa missão de patrulha de 8 horas, consome 8.71 kg de combustível.

Palavras Chave

Projeto de Aeronaves, Veículo Aéreo Não-Tripulado, Guerra Anti-Submarina, Sensor de Anomalias Magnéticas, Otimização Paramétrica

Contents

List of Figures

List of Tables

Listings

Greek Symbols

α	Angle of Attack
η_{prop}	Propulsive Efficiency
Γ	Dihedral Angle
Λ	Sweep Angle
λ	Taper Ratio
μ	Dynamic Viscosity
μ_0	Magnetic Permeability of free space
ν	Kinematic Viscosity
ρ	Air density

Roman Symbols

a	Sound speed
AR	Aspect Ratio
B	Magnetic Density Flux
b	Wing span
C	Specific Fuel Consumption
C_f	Skin Friction Coefficient
C_D	Drag Coefficient
C_{D_i}	Induced Drag Coefficient
C_{D_0}	Parasite Drag Coefficient
C_{D_w}	Wave Drag Coefficient
C_L	Lift Coefficient
C_l	Airfoil Lift Coefficient
c	Wing chord
$\bar{c}$	Mean Aerodynamic Chord
D	Drag
E	Endurance
e	Oswald Efficiency Factor
F	Force
f	Fineness Ratio
$\mathcal{F}$	Form Factor
g	Acceleration of Gravity
H	Magnetic Field Strength
L	Lift
l	Moment arm
M	Moment
m	Mass
M_0	Aerodynamic Pitching Moment

M_a	Mach Number
n	Load factor
P_t	Horizontal Tail Lift
P_{sup}	Power supplied
Q	Interference Factor
R	Range
Re	Reynolds Number
S	Wing Area
SF	Safety Factor
T	Thrust
$TSFC$	Thrust Specific Fuel Consumption
t	Thickness
t/c	Thickness-to-chord ratio
V	Aircraft Speed
V_∞	Free-stream velocity
x	Coordinate on x-axis
W	Weight
y	Coordinate on y-axis

Subscripts

cr	Cruise
f	Fuel
h	Hover
r	Induced
i, j, k	Index
ltr	Loiter
$prop$	Propulsive
TO	Take-off
∞	Environmental

Acronyms

ASW	Anti-Submarine Warfare
CfAR	Centre for Aerospace Research
CFD	Computational Fluid Dynamics
CG	Center of Gravity
CW	Counterweight
DRDC	Defence Research and Development Canada
MAC	Mean Aerodynamic Chord
MAD	Magnetic Anomaly Detection
MAD-XR	Magnetic Anomaly Detection - Extended Role
MIU	Modular Interface Unit
MSU	Modular Sensor Unit
MTOW	Maximum Take-Off Weight
NACA	National Advisory Committee for Aeronautics
NRC	National Research Canada
NSERC	Natural Sciences and Engineering Research Council
SM	Scalar Magnetometer
UAV	Unmanned Aerial Vehicle
UVIC	University of Victoria
VM	Vector Magnetometer
VTOL	Vertical Take-Off and Landing
WWI	World War I

1

Introduction

Contents

1.1 Background and Motivation

Since the first flight, human race has never stopped to go further on the quest for higher skies. In less than 100 years, Mankind was able to develop machines that fly thrice the speed of sound, to land on moon and to generate autonomous flying machines, commonly called Unmanned Aerial Vehicles (UAV).

UAV's have a enormous potential to carry any kind of mission or task. With the continuous developments in technology, these vehicles were able to match the capabilities of man-controlled aircraft. The latter, however, have a large constraint upon its design, regarding the physiological limits of human beings. Removing the human factor, it is possible to develop machines that can be applied in almost kind of operation without the necessity to install special systems, that ensure the crew's health is safe. It also allows these machines to be smaller and compact, which typically reduces the effective costs per flight hour [1].

Armed Forces can profit a lot with the development of this systems. As for patrol and surveillance operations, war conflicts or cargo drop over a war scenario, the human factor has always been a constraint, as for the risk of losing human lives, as for natural necessities.

In the Military, in case of a conflict, knowledge over the enemy is a huge advantage, because knowing the enemy position and/or tactics can dictate the success of an operation. To decrease the chances of being surprised, it is important to keep a constant surveillance over the territory in charge. For countries with large coastal areas, the ocean hide many threats, as it houses ships and submarines, which nowadays, carry large weapon capabilities.

Patrolling the ocean is a mission that typically lasts for considerable time and requires a large crew. This kind of mission could cost less if performed by UAV's, since they have lower fuel consumptions and do not require any crew on board. In the same scenario, is common to verify these manned aircraft also have anti-maritime warfare (AMW) and anti-submarine warfare (ASW) capabilities. However, for the latter, to be effective, they need to fly at very low altitudes, allowing themselves to be detected, if some object lies beneath surface.

Submarines are not a new threat and recent technologies allow these machines to be more dangerous, having longer underwater dives, heavier weaponry and longer overseas endurance. In fact, in the last years many countries have invest in submarines and in the development of their stealth and diving capabilities.

Figure 1.1 is relative to study conducted in the number of these machines around the globe and it shows that almost every country in the top-4 has two times the number of vessels of the fifth, in the list. This means that the most powerful countries, in military terms, are investing strongly in these vessels.

Attending to the general advantages of using aircraft to perform maritime surveillance and the risk of having a crew on board, it is adequate to think UAV's should perform these type of operations.

The present work contains a study of a UAV modification to perform maritime patrol and submarine

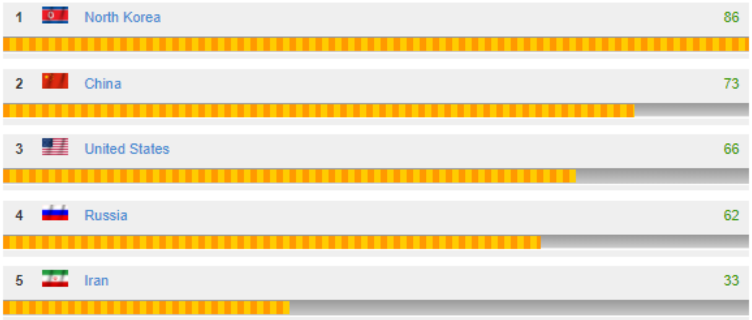

Figure 1.1: Countries with most submarines in the World [2]

detection, using a Magnetic Anomaly Detection (MAD) sensor.

1.2 Project Description

The project entitled "UAV Based Magnetic Anomaly Detection System for Remote Sensing" is a Natural Sciences and Engineering Research Council (NSERC) project in collaboration with Defence Research and Development Canada (DRDC), CAE Inc, the University of Victoria (UVic) Centre for Aerospace Research (CfAR), and assisted by National Research Council (NRC) Canada and Aeromagnetic Solutions Inc. The project goal is to develop an aircraft to perform maritime surveillance and patrol, capable of detecting submarines using a Magnetic Anomaly Detection (MAD) sensor.

It is desired to be able to vertically take off from ships or aircraft carriers, perform a patrol operation over a specified target area and return to the initial take-off point, performing a vertical landing, in a maritime environment. In the end, the operation mission profile will involve multiple UAVs conducting independent MAD searches, with the goal of detecting submerged metallic vehicles.

For this work, both sensor and aircraft were already defined prior the initialization of this thesis. These are characterized in detail in Chapter 2.

1.3 Objectives and Methodology

The primary goal of this project is to successfully instrument a UAV with a sensor capable of measure magnetic anomalies (MAD), for submarine detection.

Therefore, the purpose of this thesis can be divided into two objectives

- Assess the best position to fit the sensor in the UAV, attending different constraints and requirements;
- Evaluate the chosen configuration and possible solutions to carry the required mission, attending to aerodynamic, dimensional and operational constraints.

Using a MAD sensor for the primary mission-role, it becomes necessary to increase its efficiency to achieve higher chances of the mission's success. However, some performance aspects, such as long endurance, are also required.

Regarding the first objective, an equilibrium study of aircraft was performed, based on experimental flight data and using aircraft flight tools from UVic CfAR. Then, a parametric multidisciplinary optimization is performed to achieve the required goals, using a script MATLAB®.

1.4 Thesis Outline

This report has another four chapters, which are briefly described in the following paragraphs.

Chapter 2: MAD Operations makes the link between some theoretical and practical aspects of this subject and the project. It starts with an explanation on this kind of operations and how they have begun, and making an overview of general applications. Because the intent is to use a magnetic sensor, a quick recap on some major concepts of magnetics is given, for a better understanding. After a short recall on submarine history, an analysis of the developments in anti-submarine warfare (ASW) is conducted, along with submarine design developments, making emphasis on detection methods and why MAD sensors were brought to this field. Finally, the platform, the sensor and project requirements will be described, ending the contextualization part of this report

Chapter 3: NEBULA N1 describes the study to find the best location for the MAD sensor to be placed. Because the core of this initial study is focused on the airplane *Weights and Balance*, a short review on aircraft loads is carried for a better understanding of the process. Also, a summary of the aircraft's magnetic characterization is presented, due to requirements discussed later. After, the methodology and results of the study to install the MAD sensor onboard is discussed, showing the several approaches taken into account and criteria to choose the final configuration. The chapter ends with a model of the aerodynamics and performance is made to evaluate the aircraft's behaviour in the required operational conditions.

Chapter 4: Wing Modification: Design, Optimization and Analysis connects the requirements defined on Chapter 2 with the results obtain in Chapter 3, making possible to achieve a configuration capable of attending to all parties involved in the project. It describes the optimization process, the criteria to obtain the optimum point and makes a comparison with the aircraft at the starting point. It also characterizes the operational limits of the new aircraft and makes an estimation on the power consumption for the VTOL segments.

Chapter 5: Conclusions and Future Work ends this report, making a summary of main achievements of this project is made. It is also conducted a review about the optimizer, highlighting its limitations and its strengths. To finalize, a set of suggestions for future work is made to enhance the achievements of this project.

2

MAD Operations

Contents

2.1 State of the Art

2.1.1 Magnetic Theory Review

Magnetism is one of the oldest phenomena known by man [3]. In 800 B.C., the Greeks observed that a particular kind of stone, nowadays named magnetite, displayed a force that attracted pieces of iron [4]. In fact, the closer these stones were to iron, the stronger the force would be, which is consequence of the magnetic field generated by the magnetite.

A magnetic field is generated when electrical charges are in motion [5], reason as, most of the times, this subject is referred as *Electromagnetism*. Typically, it has two main sources: permanent magnets, such as magnetite, and electromagnets [3]. The first are natural materials, where the magnetic field is generated by the internal atomic structure of themselves. Electromagnets usually consist of wire wound into a coil and the magnetic field is only produced when electric current travels through the wire[6].

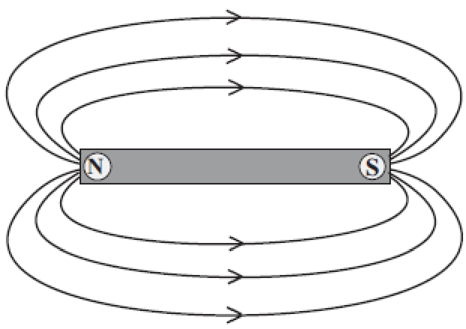

Figure 2.1: Magnetic field of a bar magnet. By convention, the lines originate at the north pole and end at the south pole [7]

There are 2 types of electrical charges: positive and negative, which when by their own, emit an electric field in all directions. Putting another charge in that field will induce a force. Charges of the same type will repel each other while opposite ones will be attracted.

In terms of magnetism, the charges are equivalent to the poles. Then, the same principle applies: to understand what causes the force, we can think of the first pole p_1 generating a magnetic field, H, which in turn exerts a force on the second pole p_2 [7]

$$F = Hp_2 \tag{2.1}$$

where $H = \frac{p_1}{r^2}$.

This means the force is proportional to the strength of the magnetic field, which is inversely proportional to the distance r between the first pole and the second [7]. In other words, strong poles induce stronger force, while larger distances between two poles weakens it. The magnetic field H is measured in Ampere per square $[A/m]$.

Another relevant parameter is the density of the magnetic flux B, which is measured in tesla T. In free space, it is linearly dependent on the magnetic field strength [8]

$$B = \mu_0 H \tag{2.2}$$

where μ_0 is the magnetic permeability of free space. Assuming that air does not have magnetic properties, μ_0 is used to characterize magnetic fields on Earth [4]. This means that either B or H can be used in this purpose [8]. In this report, all mentions of magnetic fields refer to magnetic flux density B, as it provides a more complete description of the magnetic field [3].

Magnetic fields are typically described as vector field[3]. This means that, if considering $B_1 = -4T$ and $B_2 = 4T$, the magnetic field intensity is the same in both cases. The signal refers to the orientation, which, in this case, means they are in opposite directions[1].

2.1.2 MAD Principles

Going backward on humankind history, it is known that magnetic compasses had been in use since the second century B.C. by the Chinese, and arrived in Europe in the late 12th century, becoming an indispensable tool for maritime navigation [9]. The magnetic field was the first property attributed to the Earth as a whole, aside from its roundness, by William Gilbert, who published the first book about this subject in 1600 [9].

Centuries later, technological advancements have enabled the invention of many devices capable of measuring Earth's magnetic fields, which exists due to the fact that the nucleus core of our planet is filled with molten iron. As the association between magnetite and base metal deposits was better understood, demand for more sensitive instruments grew. Until World War II, these instruments were mostly specialized adaptations of the vertical compass (dipping needle), although instruments based on rotating coil inductors were also developed and used for magnetic surveys [10].

Knowing how to measure the amount of magnetic minerals and associated rock types, it is possible to map the magnetic field intensity at any point of the Earth's surface. This mapping is usually done on magnetic surveys and can be conducted either from the air or on the ground with a magnetometer. An airborne survey can be used to map out a broad structural framework over a large exploration area, both quickly and effectively. A ground magnetic survey is used for a closer investigation, to better define and confirm any anomalies found during the airborne survey [11].

Ground and airborne magnetic surveys are used at just about every conceivable scale and for a wide range of purposes, such as mineral exploration and precious metals, and also have an important economic application, especially in oil and gas exploration [10].

Typically, aircraft used in aeromagnetic surveys are designed so their control systems and general avionics does not reduce the efficiency of the sensor. During flight, these system are sources of magnetic noise that may cause inaccurate measurements. One way to avoid this is to put sensor as far as

[1] For further detail, please check [3] [4] [7]

possible from this components or to isolate it from a magnetic perspective, using non-magnetic materials as much as possible when manufacturing or installing those components.

(a) Stinger boom

(b) Towed

(c) Wingtip

(d) On top of fuselage

Figure 2.2: Examples of aircraft configurations for airborne geomagnetic surveys

On Figure 2.2 several configurations are displayed. These are defined through attending to the aircraft flight qualities, sensor safety and efficiency. On of the most common is the stinger configuration, which guarantees enough clearance for the sensor, from a magnetic perspective. However, when used on helicopters, it should be noticed that an instantaneous gust may pitch the aircraft. If long enough, the boom can approximate to the rotor axis, which may endanger the structure and the rotor itself. The towed configuration also guarantees magnetic clearance, however it puts the sensor in a much vulnerable position regarding atmospheric conditions. The wingtip configuration is typically used on aircraft with low magnetic signature on board the fuselage or high span wings, which, alongside the wingtip pods, have consequences on the aircraft flight qualities.

Knowing the typical behaviour of the Earth's magnetic field, it becomes simple to deduce that any disturbance has an associated cause. Magnetic anomaly detection (MAD) is a method that has been used for decades and has been successful in detecting ferromagnetic objects. Because air, water, and most soils are practically transparent to the static magnetic field and indifferent to weather conditions, MAD became especially attractive for detecting hidden targets [12]. By exploiting the magnetic anomaly produced by an object in the Earth's magnetic field, several applications have been developed to make use of this method, especially in the military [12]. Common applications include submarine detection and, potentially, land-based surveillance. By being a passive method, it can stay unrevealed to its target, which is an advantage over others active sensors, such as radar [13]. In addition to traditional military applications, MAD sensors are also suitable for para-military and civil applications such as drug interdiction, power line monitoring, tunnel detection, and magnetic surveys [14].

Because the intent is to focus on submarine detection, it will be used as an example of how a metallic object affects the geomagnetic field, allowing a particular device to detect those anomalies.

The lines of force in a magnetic field can make the transition between air and ocean almost undisturbed because they pass through both water and air in similar manners. Therefore, a submarine beneath the ocean's surface distorts the earth's magnetic field, enabling its detection from a position in the air with a MAD sensor [15].

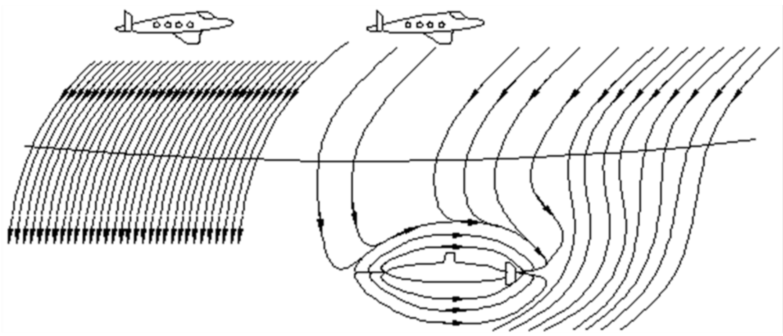

Figure 2.3: Typical geomagnetics vs anomaly caused by a submarine [16]

This distortion is due to the submarine's ferromagnetic properties and fabrication process. While the submarine hull is being fabricated, it is subjected to heat (welding) and to impact (riveting). Ferrous metals are the most common type of material used in this process and contain groups of iron molecules called "domains." Each domain is like a tiny magnet, having its own magnetic field, with a north and south pole. If the domains are not aligned with any axis and pointing random directions, the magnetic field generated is negligible. However, during welding and riveting, particles are agitated, and the metal produces a constant magnetic field, which causes the domains to orientate themselves opposed to the geomagnetic field, i. e., their north pole towards the Earth' south pole and vice-versa. In that situation, all domains have an additive effect. Because a submarine's hull contains so much steel it acquires a significant permanent magnetic field [15].

The total magnetic field or "magnetic signature" of a submarine at any point on the Earth's surface is the sum of its permanent and induced magnetic fields, i. e., Earth and ship, respectively [15].

The function of airborne MAD equipment is to detect anomalies in the earth's magnetic field, caused by these vessels. A ship's magnetic field may be reduced, but for practical purposes, it is not possible to eliminate such fields entirely [15].

2.1.3 Anti-Submarine Warfare

Just as flying, the idea of long travels below the water surface has always been present in the human mind. Ancient legends tell Alexander, the Great adventured himself on a glass vessel, more than 2000 years ago. After that, only halfway through 16th-century, new leather insulated wooden vessels were drawn, by British naval officer William Bourne, although were never proven to work [17].

As time passed by, technological developments allowed the French to build the first submarine to use a diesel engine on the surface and an electric engine below, in the early 20th-century [17]. During WWI, Germany's U-boats proved war could be made using the depth of the ocean. As they were recorded to be responsible for the sinking of more than 10 million gross tons of Allied ships during the Battle of the Atlantic [17]. These attacks were mainly aimed at merchant shipping and would have cut off the Allied forces lifeline if the United States of America had not made their entrance in the conflict. They allowed the creation of a convoy system, in which naval warships and land-based anti-submarine warfare (ASW) aircraft protected those vessels [18]. At this time, methods to attack submarines were rudimentary and dependent on it surfacing or giving away its own position, so opportunities were limited [19].

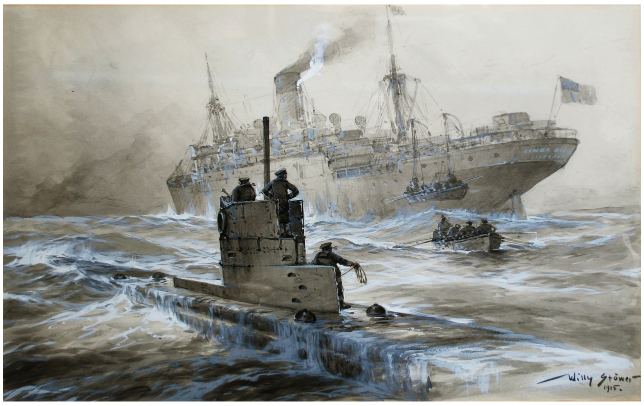

Figure 2.4: *Sinking Of The Linda Blanche Out Of Liverpool*, by Willy Stoewer, 1915. The Linda Blanche was sunk on 30 January 1915 after an German U-boat attack [20]

In the current days, and in wartime conditions, there are five phases of ASW used to summarize an ASW scenario. These are [18]:

1. Detection – the submerged object has been observed with a single sensor

2. Classification – a judgment of the object is passed based on multi-sensor information

3. Localization – when classified as a submarine, its accurate location is determined

4. Tracking – accurate location information is obtained over fixed time intervals, to determine a submarine course

5. Attack – if necessary, determination of the best application of weapon systems to eliminate the submarine threat

For submarines, it is crucial to stay undetected, to avoid the risk of being destroyed by the enemy, compromising the mission's success. Early submarines had the advantage of being ahead of this countermeasures, by using the vastness of the ocean. One of the biggest turning point for submarine detection came with echolocation, when sonar (sound navigation and ranging) devices were introduced to this field. This technological innovation was able to reveal objects and landscape below the water's surface by measuring the timestamps difference between an emitted sound wave and its recorded reflection. Knowing the sound speed at those conditions, is possible to create a sound signature, as shown in Figure 2.5, to estimate the distance to the detected object. This method is called active sonar, and it is similar to radar (radio detection and ranging), although the latter uses radio waves instead. Active sonar sources and receivers, which are essentially underwater loudspeakers and microphones, are usually distributed along a rope in an array and towed behind a ship [21] [22].

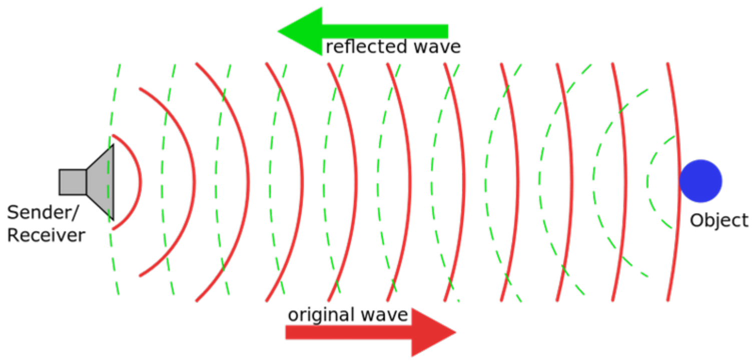

Figure 2.5: Echolocation process. Adapted from [21]

However, this task is much harder than what it looks. Submarines can avoid being detected by diving close to shore shallows, where the ambient noise generated by coastal waters, undulation, marine life, and other maritime vessels make sonar detection extremely difficult [23] It has also been proven sonar use is associated with the death of marine life, so ships can't use it within 12 nautical miles of the coast [22] [24].

When travelling in open-sea, the task does not become easier. In order for sonar work properly, submarines need to have a good reflective steel surface and be where the water temperature is constant. In the ocean, the water level of salinity and temperature vary, which causes variations in sound waves' speed [21] [25].

Additionally, if the water temperature and salinity are constant, the sound velocity increases with hydrostatic pressure, which increases with the depth [25].

Typically, there is a surface layer warmer than the water beneath it, known as mixed layer. Below it, the water rapidly grew colder with depth. Knowing that the speed of sound increases with temperature, sonar signals travel quickly through the warm layer and slow dramatically when they hit the cooler layer below.

When passing the border between layers, there is a refraction in sound waves, bending them away from the region where sound travels faster and toward the region where its speed slows. This bending creates an acoustic “shadow zone”, allowing any submarine to become invisible to sonar signal, when positioned just beneath the dividing line between the warmer and cooler layers of water [2] [25] [26], as shown in Figure 2.6.

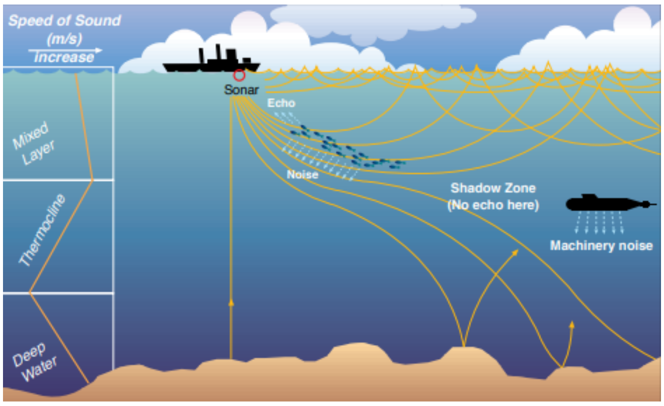

Figure 2.6: Propagation of sound waves in the ocean [27]

With all these difficulties, another way to use the sonar is just by simply listening to the environment around. A moving body disturbs the water, leaving an imprint of sound waves that can be detected by the pursuer’s highly sensitive microphones. This is called passive sonar [21] [28].

However, technological advances allowed submarines to be incredibly quiet while travelling underwater. In the last century, the noise level generated by an underwater vessel decreased, as can be observed in Figure 2.7.

Although the chart is qualitatively scaled regarding the noise level, it is clear to verify two of the most powerful countries in the world, USA and Russia (former USSR), have been focussing their efforts in decreasing the sound signature of their underwater vessels.

Despite submarine design achieved several milestones to decrease the sound signature, the hardest task still is to keep the main sources of noise, such as machinery for air circulation inside the vessel and the engines, as silent as possible[21]. Nowadays hybrid diesel-electric submarines were granted capability to use the electric engine to move at low speed and diving, when submerged, decreasing their

[2] For detailed information about this phenomena, please check [25] and [26]

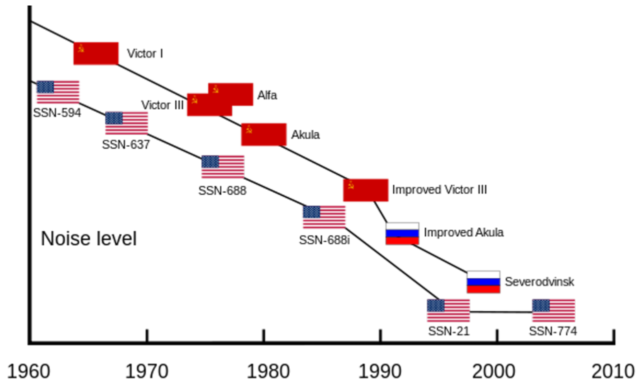

Figure 2.7: Sound signature level evolution comparison between vessels from USA and Russia, in the past century[21]

sound signature[22].

All these facts and countermeasures created a necessity to find other solutions to increase the success of classification phase, as it became extremely difficult to make a correct judgment of the sea environment, just by using sonar.

ASW is a fusion of technology and tactics [8]. It involves, in many cases, maritime and aerial means, and several kinds of sensors, to increase the chances of success.

Figure 2.8: Philippine Navy P-3 along a ship on a ASW training exercise [29]

Sonar is still the primary sensor on detection phases and has the support of many secondary sensors, which include: magnetometry, radar, infrared imaging and electronic support measures [18].

Despite all the progress made, most of the submarines external hull main components are made of ferrous materials, such as steel, so they can stand the enormous external pressure while submerged. This fact allows magnetometry to be used, as explained in 2.1.2.

Typically, naval ships are not equipped with MAD sensors because most of its structure is made of steel and other ferromagnetic materials. These generate an induced magnetic field that causes a decrease in the sensor's efficiency and may give an inaccurate analysis of the external environment. Therefore, ships are usually equipped with sonar, while aircraft, manned or unmanned, can carry several types of equipment, associated with these distinct methods.

Additionally, ASW aircraft can have multiple capability levels within all five phases. For instance, nowadays state of ASW has UAVs focused in detection, localization, and tracking stages, while manned ASW aircraft maintain capability in all five phases.

One of the most successful aircraft in maritime surveillance and patrol operations is the Lockheed P-3 Orion. With the ability to stay in the skies up to 12 hours and to be equipped with multiple sensors and weapons, such as torpedos, this aircraft is still employed by many nations, despite being introduced in the 1960s [30] [31]. A distinct characteristic is a tail stinger boom, as shown in Figure 2.9, designed to carry a MAD sensor, allowing it to be distanced from the avionics and other systems that may cause high levels of magnetic interference. It also can be equipped with multiple sonobuoys, an expendable sonar system that is dropped into the ocean during flight [32].

Figure 2.9: Portuguese Air Force P-3 on a low pass. Stinger boom highlighted in the red contour. Adapted from [33]

MAD sensors are typically employed as a secondary sensor in the localization phase. However, with the strong decay of target magnetic fields, ASW aircraft must fly at lower altitudes to enable detection. This increases the risk of the aircraft to be detected by submarines, due to noise and vibrations, reason why, most of the times, MAD is reserved for later phases of ASW [18] [8]. A way to avoid detection by submarines is to fly smaller aircraft, like UAVs, as their reduced dimensions and engine cause less noise and air disturbances during flight, when compared to larger aircraft.

2.2 Project Description

2.2.1 Aircraft Characterization

The *NEBULA N1* was the aircraft chosen to accomplish the proposed mission. This vehicle is an unmanned aircraft developed by NEBULA Unmanned Aerial Systems.

The UAV, shown in Figure 2.10, is a modular high-wing monoplane, with a tractor propeller and high T-tail, fabricated using composite materials. A series of custom-manufactured processes were conducted on its airframe to enhance the wings' stiffness. The reduced volume of ferromagnetic materials in the airframe was one of the reasons to choose this aircraft for the project.

Another reason regards its versatility. Designed to have a modular tractor propulsion system, this

Figure 2.10: N1 disassembled at UVic CfAR' shop

aircraft can be modified into several propulsive configurations:

1. Electric Propulsion, with one or two batteries, depending on the flight profile required;
2. Gas Propulsion;
3. Any of the above coupled with 2 electric motors on each wing, giving it VTOL capabilities, as shown in Figure 2.11.

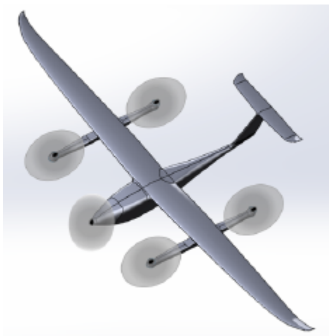

Figure 2.11: Nebula N1 VTOL computational model

At the time this project was conducted, the N1's propulsion system was electric, requiring a pneumatic launcher, as displayed in Figure 2.12, and landing via belly touchdown, which required a smooth field to not compromise the aircraft structural integrity.

In Table 2.1, a summary of the aircraft general parameters is shown:

Depending on each configuration, the N1's performance parameters change. Higher endurance and flight speeds are achieved using the gas propulsion system when compared the maximum registered in the electric configuration, even if two batteries are used.

Typically, when powered by one battery and flying at 24 m/s, the N1's endurance is approximately 1 hour.

Figure 2.12: NEBULA N1 mounted on pneumatic launcher[34]

Parameter	Value
Cruise Speed $[m/s]$	26
Wing Area $[m^2]$	1.035
Wing Span $[m]$	3.9
Fuselage Length $[m]$	2

Table 2.1: NEBULA N1 parameter summary

The intent is to use the N1 during initial flight testing and concept validation, regarding the configuration adopted for the installation of the sensor onboard.

2.2.2 Sensor Description: MAD-XR

The MAD-XR (Magnetic Anomaly Detection - Extended Role) is a newest generation sensor, developed by CAE.Inc. With an huge advantage of being compact, this military-grade MAD sensor has reduced weight and size, and its power requirements allows it to be incorporated in a smaller aircraft, such as UAVs [14].

Figure 2.13: MAD-XR [14]

The MAD-XR performance was proven, in flight test, to be similar to another CAE's larger sensor, the AN/ASQ 508 MAD system, installed in larger maritime patrol aircraft, like the Lockheed P-3 and Boeing P-8 [35]. In Table 2.2 a comparison between the systems is conducted to highlight the reduced dimensions and mass of the MAD-XR.

The whole system can be divided in four components [36] [37], as shown in Figure 2.14:

Parameter	AIMS AN/ASQ 508A	MAD-XR
Weight	Approx. 27kg	Approx. 1.5kg
Size	23cm (diam) x 100 cm	15cm (diam) x 24cm

Table 2.2: Comparison of each sensor's characteristics [14]

- Vector Magnetometer (VM) - Measures the transverse, longitudinal and vertical components of Earth's geomagnetic field, with relationship to aircraft's position and orientation to compensate its manoeuvres;
- Scalar Magnetometers (SM) - Sense the total magnetic field, monitoring changes in the earth's magnetic field due to anomalies in the surrounding environment;
- Sensor Module (MSU) - Design to be the attachment point between the system and vehicle, it gives structural strength and works as protective shell for the magnetometers described previously;
- Interface Unit (MIU) – Performs sensor control, digital data acquisition, health monitoring and provides digital inputs to an on-board processing unit or to a ground station via the UAS digital link

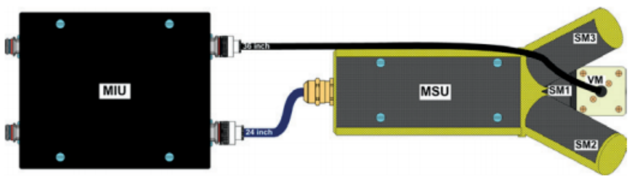

Figure 2.14: Scheme of MAD-XR full system [36]

Although not constant, the range of this MAD system will generally detect anomalies at approximately 1200 metres [14], which is a crucial factor to determine the flight altitude.

2.2.3 Requirements

As explained in the beginning of section 2.2, various entities were involved in this project. During the time this thesis was conducted, several discussions took place among stakeholder to determine project specifications and constraints, so the most suitable configuration to every entity is obtained.

2.2.3.a) Magnetic Signature

To maximize the sensor's performance, it must be placed such the amount of magnetic interference generated by the aircraft is minimized. In airborne magnetometry, the whole aerial system must go through aeromagnetic compensation to eliminate self-generated interference effects [38], such as component demagnetization or replacement for non-magnetic material. However, the largest amount of magnetic noise is generated when manoeuvring [10], so the aircraft should have stiffeners to reduce vibrations and relative motion. Hansen [8] performed a static characterization of the aircraft that will be explored on the next chapter.

2.2.3.b) System Constraints

As discussed in section 2.2.2, the MAD-XR is composed by two components: the sensor itself and an interface unit, responsible for the data logging and analysis. According to the manufacturer, the distance between these devices must not exceed 2.5m. None of these has any specified orientation, although it is recommended for the MSU to be aligned with the aircraft's longitudinal axis (in this case, to be parallel with the fuselage).

The interface's mass is approximately 650 grams and the harnessing between this unit and the MSU weighs, approximately, 200 grams per meter.

2.2.3.c) Flight Operations

In a patrol operation, the goal is cover the maximum area as possible to increase the chances of success. Typically, these types of mission are characterized by a target loiter time over a designated search area, away from the take-off point, as shown in Figure 2.15.

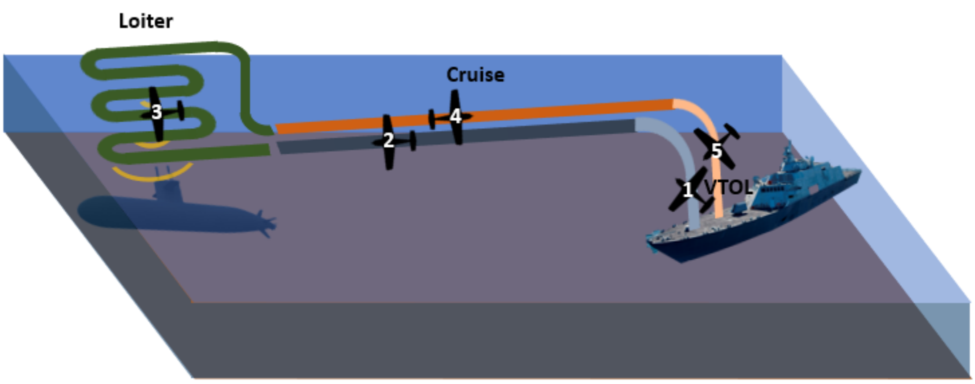

Figure 2.15: Target Mission Profile

For this project, the performance and operational goals were the following:

1. Vertical take-off from a ship over the ocean;
2. Cruise for 20 nautical miles at 50 m/s;
3. Perform patrol/search mission for 4 to 8 hours, at 40 m/s;
4. Dash back in same conditions as item 2;
5. Vertical landing at the initial point.

Depending on the aircraft performance and aerodynamics, the cruise and loiter altitudes may differ. Due to the conceptual nature of this study, an equal altitude of 300ft (approximately 100m) for these stages was considered. This value allows the aircraft to fly as low as possible without compromising its own safety. Also, submerged targets could be at a significant depth, thus lower altitudes always provide better chance of target detection.

To achieve these objectives, the N1 will be modified towards an hybrid propulsion configuration, having a combustion engine and fixed-pylon electric motors as sources of thrust, as shown in Figure 2.11.

The VTOL system will be used to only for take-off, landing and the transition phases between these and horizontal flight. In cruise and loiter stages, it would be shut-downed, making the N1 perform like a conventional fixed-wing aircraft.

3
NEBULA N1

Contents

3.1 MAD-XR Location Assessment

3.1.1 Magnetic Signature

As previously said, Hansen [8] characterized the magnetic properties of the aircraft, measuring the intensity of the magnetic field of each component in the field using magnetometers and using *COMSOL*, a finite element software.

According his analysis [8], the main sources are enumerated, as follows, in order of significance: propulsive units (combustion engine, VTOL motors, ext), servos/actuators (flight control, gas throttle), assorted avionics and ferromagnetic fasteners, as shown in figure 3.1.

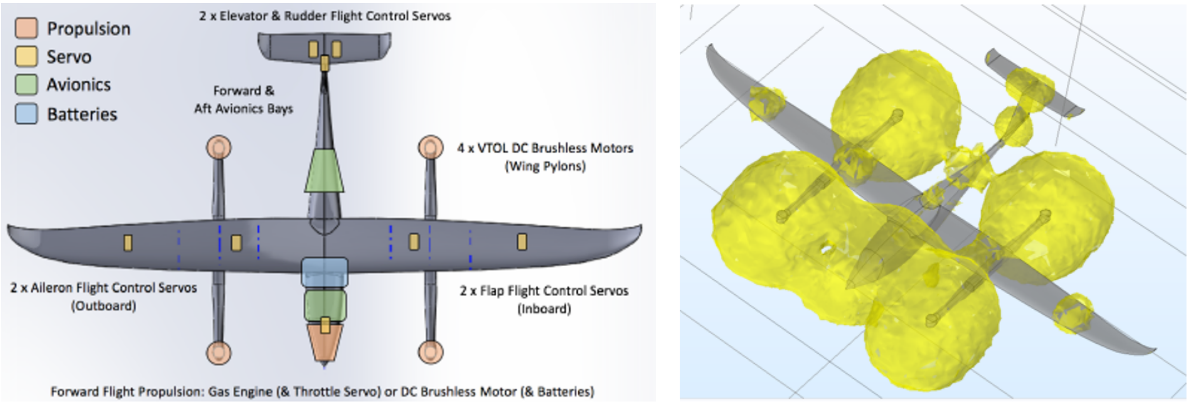

(a) N1 component display

(b) COMSOL model analysis

Figure 3.1: On the left, figure 3.1(a) shows the main sources of magnetic noise; On the right, figure 3.1(b) shows the *COMSOL* analysis of the magnetic field's intensity generated by each component. Adapted from [8]

To respond to this issue, many configurations were considered, based on another aircraft and similar studies, as seen in figure 2.2. However, due to the nature of the project and objectives, some of them were discarded because of their unfeasibility, in terms of aerodynamics, sensor's efficiency or overall structure.

Onboard fuselage configuration was quickly rejected given the presence of the high levels of magnetic noise, generated from the VTOL motors and engine, near the fuselage, as shown in figure 3.2. Large engineering and time costs to compensate the amount of interference made this option unfeasible.

The towed configuration has the advantage of maximizing distance from the aircraft but suffers from movement induced noise, positional errors, additional aerodynamic drag and a risk of damaging the magnetometer due to external weather conditions [8]. The large number of disadvantages compared to the benefits made this configuration to be disregarded.

Therefore, only conventional fixed-wing MAD configurations were considered, in which options were

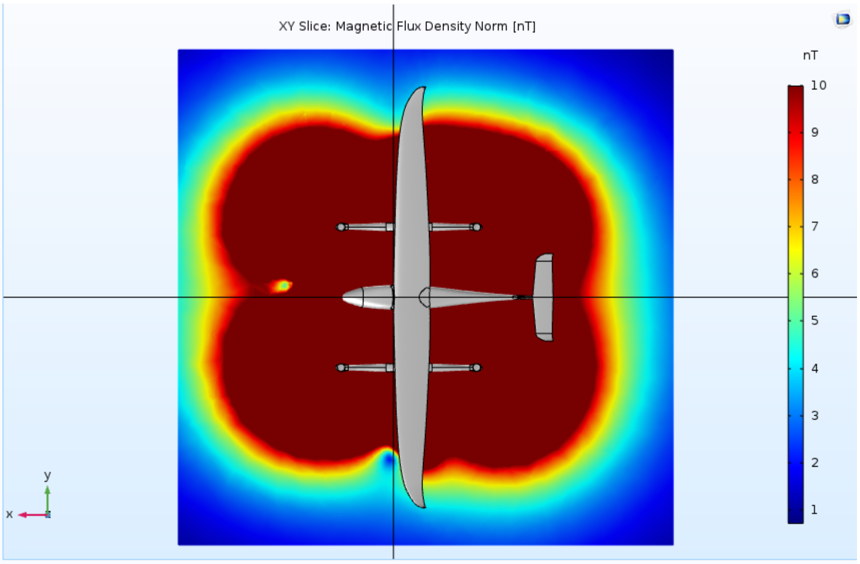

Figure 3.2: Intensity of the aircraft's magnetic field [8]

a wingtip placement or a "stinger boom" at the tail. Hansen [8] used the aircraft magnetic signature models and made a prediction on the magnetic noise at these potential MAD locations. The following topics are a summary of the results from the analytical and computational model for each configuration.

3.1.1.a) Wing Tip

Due to the low proximity to the wing's control surfaces' actuators and VTOL engines, the N1's right wingtip showed the least value of magnetic noise over any other point in the aircraft, having a total magnetic field of -2.9nT. See figure 3.3. The asymmetry relatively to the left one is due to a magnetic shunt located on the left side of the aircraft's nose, right next to the engine.

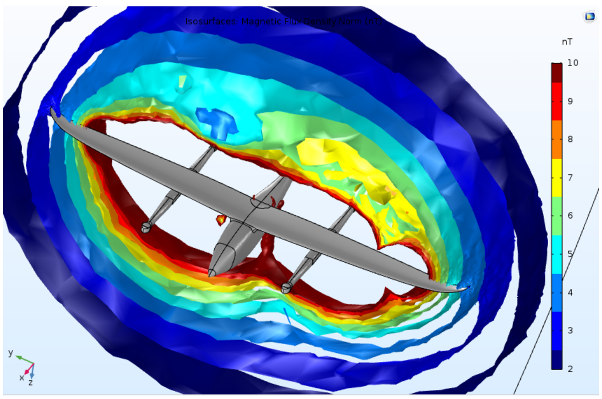

Figure 3.3: Measurement of magnetic field intensity at the wing plane [8]

Another conclusion from Hansen analysis was that any displacement in the longitudinal direction, i. e., perpendicular to the wing span, at the wingtip did not substantially change the value of the magnetic flux. This means that only structural and aeroelastic effects on wing should be consider upon its modification.

3.1.1.b) Tail Stinger Boom

Although the aircraft's tail is distanced from the VTOL engines, it suffers huge effects of magnetic noise from its control surfaces' actuators. This area has an unexpectedly high level of interference, due to the fact it is being right under the rudder and the elevator servo actuators, which have a 96% contribution [8] among all sources of magnetic noise in the aircraft.

To make a suitable comparison, it was made an assessment of how far from this point the sensor should be place, in order to, at least, match the lowest level of magnetic noise measured in the wingtip.

According to Hansen's model, the tail boom should have a minimum length of 0.4m, counting from the tail empennage, as shown in figure 3.4, with a white-coloured arrow.

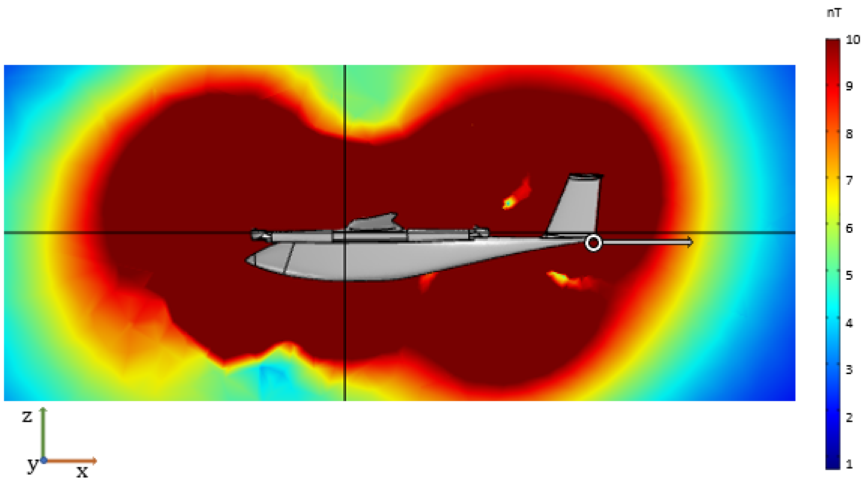

Figure 3.4: Analysis of the general magnetic field around the aircraft for tail stinger boom configuration. Adapted from [8].

In this case, the computational analysis was not coincident with the analytical model, with error between them being relatively high. However, according to the author, given the complexity of the magnetic interactions and the undefined far-field, these results were generally accepted as valid [8]. At the time of this computation, it was not clear what the minimum length should be according to the computational model, so the result from the analytical one was taken as an object of study for the next phase.

3.1.2 Initial Study: Sensor Integration

In this section, it is shown how the study to choose the best configuration was conducted, considering the aircraft stability and the influence of magnetic interference, previously discussed.

In these types of aircraft, controlling the weight is a critical factor, due to the fact it has a direct influence in the aircraft's performance and stability. Before present the methodology carried out during the sensor integration in terms of equilibrium, is conducted a review on aircraft static stability for a better understanding of the challenges encountered.

3.1.2.a) Aircraft Aerodynamic Review

It is quite impressive to see an airplane, a large and heavy body, moving almost as freely as a bird in the sky. *"How is that possible?"* is probably the first question it comes to mind when watching such thing.

In fact, the reason why this happens is due to the existence of air in the atmosphere. Air is composed by gases, which, according to White [39], have the behaviour of a fluid. When a body is moving through a fluid, it is subject to two interactions: *pressure*, due to molecules displacement, and *shear stress*, due to friction between the body surface and the fluid particles [40]. This interactions occurs all over the body shape, with pressure acting perpendicular to the surface and shear acting parallel. The integration of these over the total surface will result in load called Aerodynamic Force R. Now, let's think it is the fluid that is in motion, just like a windy day. The same interactions verify and in this case, the body is being subject to a free-stream, with a certain velocity V_∞ [40]. By definition, this load is decomposed into two main components: a parallel to the free-stream called *drag* and a perpendicular, called *lift* [40].

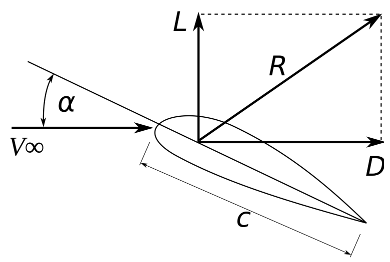

Figure 3.5: Aerodynamic Force decomposed on Lift and Drag loads. Adapted from [40]

The wing section represented in Figure 3.5 is inclined. This inclination is called *angle of attack*, α, and is the angle between the free-stream and the wing *chord*, the straight-line distance between the aircraft leading edge and trailing edge [40].

When contouring a wing, the fluid motion generates a difference in the pressure between its upper and lower surfaces. They are designed in particular shapes to make the flow increase the local pressure on lower surface and decrease it in the upper surface, on its passage. Then, the air does rest by pushing the wing upwards, originating the lift load. The same phenomena occur in other bodies. For instance, on an airplane, the fuselage also generates lift, but it is negligible when compared to the lift generated by the wing. Flying is only possible when the total generated lift is larger the body's weight.

During flight, aircraft are subjected to other loads apart the lift and drag forces, as shown in the next diagram.

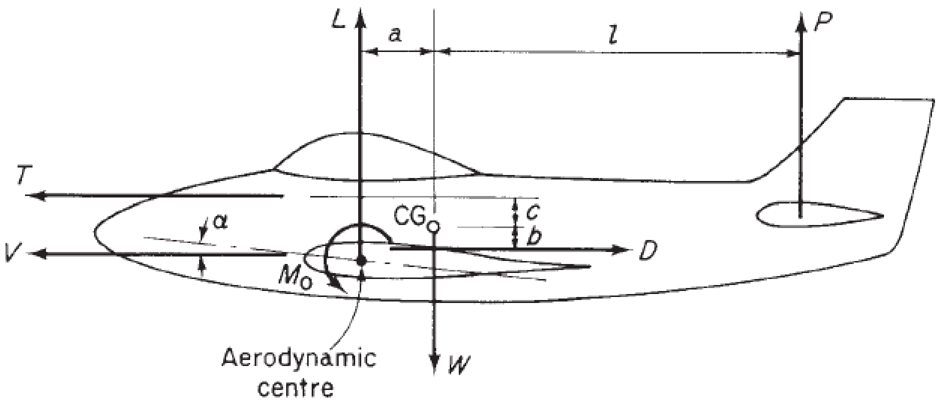

Figure 3.6: Loads on aircraft during level flight[41]

where L is the Lift force applied to the aerodynamic centre, D is the aircraft Drag, T is the Thrust, the propulsive load generated by the engine, W is the the aircraft weight applied to its center of gravity (CG), P is the horizontal tail load and M_0 is the aerodynamic pitching moment, disregarding tail's contribution[41]. V is the free-stream.

When flying in a steady level flight at constant speed, it is assumed the aircraft is in static equilibrium [41], which means

$$\sum F_x = 0 \tag{3.1}$$

$$\sum F_y = 0 \tag{3.2}$$

$$\sum M_{CG} = 0 \tag{3.3}$$

Applying the conditions on Equations (3.1) and (3.2) to the loads on the diagram on figure 3.6, is obtained

$$T - D = 0 \tag{3.4}$$

$$L + P - W = 0 \tag{3.5}$$

For moment equilibrium about the aircraft's CG, Equation (3.3) can be re-written as

$$La - M_0 - Tc - Pl - Db = 0 \tag{3.6}$$

In this study, it is assumed the aircraft equilibrium of moments is verified, taking only into account the position of the CG for the following section. Therefore, installing the MAD-XR onboard the N1 also required the installation of a counterweight, to keep the aircraft CG in the design position.

3.1.2.b) Weights & Balance

This study was conducted in both electrical and gas configuration, regarding the difference of both propulsive systems. Although not crucial for the final product, it was important to carry out this analysis because most of the initial flight test would be conducted using the electric mode. As so, it was important to verify if the best solution suited with both configurations.

The same methodology was used to characterize both system, as described next:

1. Measurement and assessment of each component's weight;

2. Study of the positioning of each component in the fuselage;

3. Analysis of the aircraft stability.

The final assessment was carried out using an *Excel* flight stability tool, developed by the aircraft's designer, used for flight test stability checking. As a convention, the referential for the components coordinates has its origin on the intersection of the wing's leading edge and the aircraft symmetry plane, as displayed in figure 3.7. Z-axis is perpendicular, in the opposite direction to the readers' sight.

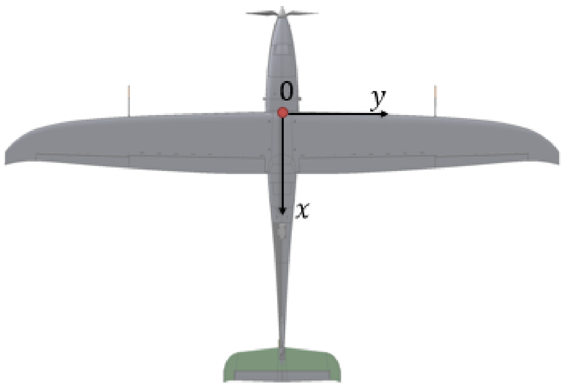

Figure 3.7: Location of the coordinate system in the aircraft

From previous operations, all base configuration components, such as the airframe and propulsion system, were already characterized and their position on the aircraft was correctly specified.

As highlighted earlier, adding a mass to an aircraft is a procedure that requires cautiousness, because it will have consequences on the performance and aerodynamics of the aircraft. According to N1 designer [34], there were two main parameters to take into account in this process:

1. The maximum take-off weight (MTOW) could not exceed 35 kg;

2. To keep the aircraft' stability, the x-position of CG should be kept between 0.140m and 0.146m.

As the name says, the aircraft's MTOW is limit weight the aircraft can have prior to take-off that guarantees the structural integrity and flight qualities it was design for.

From [34], is was known the N1's mean aerodynamic chord ($\bar{c}$) is 0.2649m and the aircraft neutral point is at $x = 0.179m$, so during the process, the objective was to keep the CG's position at $x = 0.143$m.

Knowing the sensor's mass is about 1.5kg, it was assumed the wrapping pod and mounting frame were going to be prototyped in a 3D printer and would have, approximately, 0.5kg of mass. The wire's weight was not considered on equilibrium calculations.

From this point, for nomenclature simplification, when referring to the MSU's mass, it will accounted its own (1.5kg) and the container (0.5kg), totalling 2kg for analysis.

3.1.2.c) Tail Stinger Boom

In this configuration, adding a mass to the aircraft will induce a large nose-up pitching moment, equal to the product of MSU's weight and distance to the aircraft's CG, as shown in the following equation

$$M_{MSU} = (x_{MSU} - x_{CG}) \times W_{MSU} = l_{MSU} \times W_{MSU} \tag{3.7}$$

where l_{MSU} was equal to 1.71m, defined according to Hansen's analysis [8].

In Equation (3.3), it is shown that one condition to achieve steady level flight is that the sum of moments about the CG has to be null. Taking into account the result of Equation (3.6), adding a single to the aircraft will induce a pitching moment, except if placed on the CG, which was not an option. Therefore, it was necessary to account for integration of a second mass, to cancel the MSU's moment and keep the aircraft stable when flying.

To minimize the amount of mass to be added and achieve the same moment, it was required to get the highest arm as possible. Therefore, it was decided to locate the CW next to engine mount, occupying voids in the structure, distanced 0.57m to aircraft's CG. Due to the small volume availability, it was decided to use led, profiting its high density.

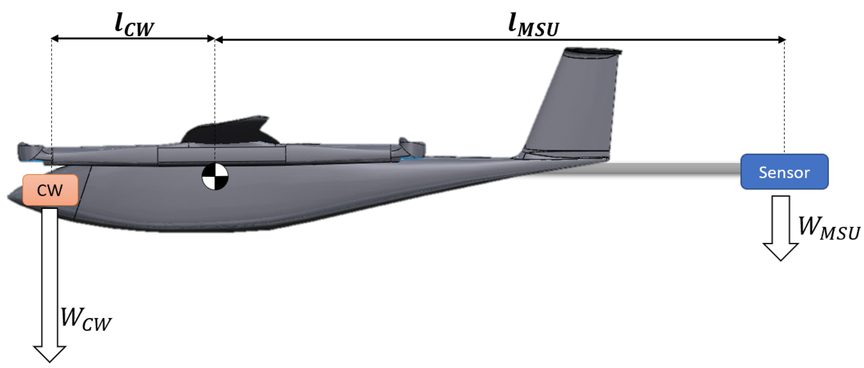

Figure 3.8: Acting loads from MSU and respective counter-weight

To compute the CW's mass, it was only necessary to apply Equation (3.3) to the diagram in Figure 3.8:

$$W_{MSU} \times l_{MSU} = W_{CW} \times l_{CW} \tag{3.8}$$

3.1.2.d) Wing Tip Configuration

For this case, the calculations were much easier, since both wingtips were going to be modified to keep the aircraft symmetry. Therefore, no additional lateral trimming was required, if the added mass on each wing was the same. Once again, led was used as counterweight for the MSU.

3.1.3 Weight Assessment

Having established the governing equations to the problem, it became simple to accurately compare these configurations. In this section, an evaluation of the amount of mass required to trim the aircraft is made for each propulsive configuration.

The airframe weighs 14.45kg, which will be added 1kg due to the MAD-XR interface unit (MIU) and respective harnessing. This measurement was conducted when the aircraft was configured to electric propulsion, so it includes the electric engine.

3.1.3.a) Electric Propulsion

When on this configuration, N1 the electrical engine power is supplied from a pack of batteries. The N1 was design to carry two of these (if necessary), each one weighing 4.45kg [34], mounted as displayed in figure 3.9. Having two batteries enhances the aircraft performance, but is not enough to perform the desired operation. Flight testing was typically conducted using a single battery.

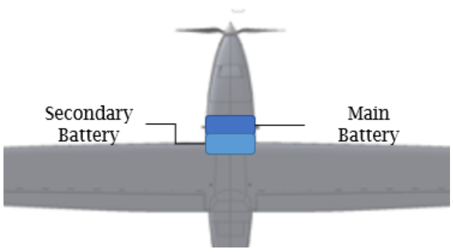

Figure 3.9: Battery Location

On the equilibrium analysis, the battery was included in the aircraft's weight, given the fact their position was already known, totalling 19.9kg for the airframe. Figure 3.10 represents the results of the computations.

As expected, the mass of the counterweight has a direct consequence to the aircraft's payload capacity. For the electric configuration, the tail stinger boom requires more than twice the mass of CW required for the wing tip. This chart suggests the wing tip solution has more benefits than the other, when taking into consideration the total added mass. However, as explained earlier, the electric mode is only used for flight testing, so, to decide which option should be applied, it was also necessary to evaluate the combustion configuration.

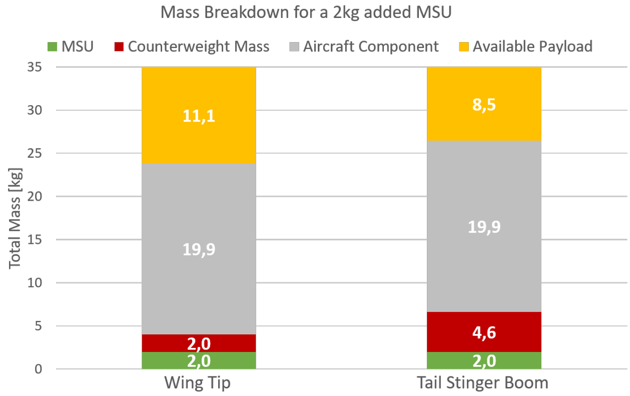

Figure 3.10: Comparison of the mass distribution of each option for the electric engine configuration

3.1.3.b) Combustion Engine

For this assessment, it was required to remove the components of the electric engine and install the combustion system.

$$m_{airframe_{comb}} = 14.7 - \text{Electric Propulsion System} + \text{Gas Propulsion Sytem} \tag{3.9}$$

From measurements, it was concluded the electric and gas system weigh 1.6kg and 5kg, respectively. For the latter, the position of the fuel tank was not already defined, although was intended to place it onboard the fuselage, coincident to the aircraft's CG. Therefore, the fuel was accounted as payload and airframe's mass equal to 18.8kg.

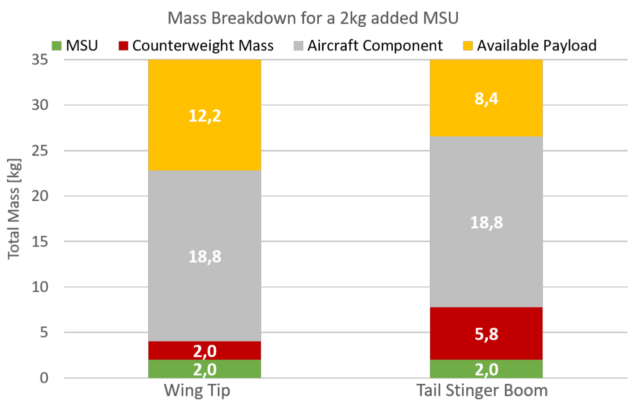

Figure 3.11: Comparison of the mass distribution of each option for the gas engine configuration

Similarly to the electric mode results, the wing tip solution is best one, since the total added mass is approximately half the added on the tail stinger boom.

3.1.3.c) Additional Aspects

From the operational point of view, there were some aspects to be considered. According to the N1's designer [34], the aircraft is able to fly more than 3 hours per kilogram of fuel, at cruise speed, reason to choose a solution that provides the highest payload possible. Also, each configuration studied had some benefits and disadvantages, as compiled in the next list:

A) Wingtip

1. Because the wing was design accounting the installation of the engine nacelles for VTOL, the structure had enough stiffness to support the load caused by the attachment of the MSU at the wingtip;
2. Easier production, since it only requires the removal of each wingtip, design and manufacturing of the container;
3. The cabling between sensor's MSU and MIU is thicker than the wing itself, which requires special maintenance and installation procedures;
4. Better aerodynamic efficiency because wig tip pods would work like a winglet [42]

B) Tail Stinger Boom

1. High risk of damage, due to ground reaction on landing;
2. Longer production time, since it requires the design of a boom stiff enough to make the harnessing of the sensor's housing structure and the aircraft's fuselage, which requires a study and manufacturing of an attachment point. Additionally, because two different designs are required (boom and container), the manufacturing time is higher;

3.1.4 Result Discussion

3.1.4.a) Analytical Results

Comparing the results from Figures 3.10 and 3.11 and the list of additional aspects described above, it was clear that the wing tip solution was the best option. One crucial factor on this choice was the amount of modifications the airframe required due to the project schedule. Additionally, the available payload in that configuration played a important role, since the avionic system and fuel still needed to be added to aircraft, regarding the combustion engine configuration. Also, it was assumed the MSU to weigh 2kg. A worst-case scenario assumption was also studied, in which the system mass was 3kg, assuming specific materials had to be used upon the harnessing and to manufacturer the container. A summary of the calculations is shown in the following graphics.

In case the MSU final mass was 3kg, the amount of mass required to cancel its moment increases almost 3kg. This means a total of 11.7kg additional mass to aircraft for the installation of a system on

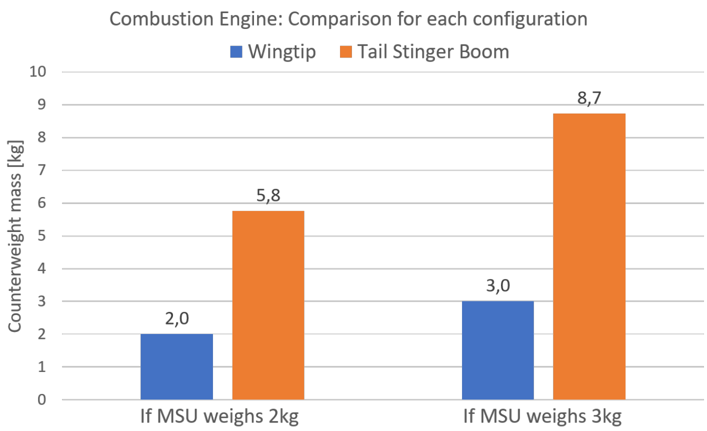

Figure 3.12: Comparison of the mass distribution of each option for the gas engine configuration

board, which would represent 33% of the maximum take-off. For the wing tip, the total mass is 6kg, since the counterweight mass will be equal to MSU. The computations only confirmed the choice of using a wing tip configuration to install the MAD-XR was the best one.

3.1.4.b) Experimental

The N1 was modified taking into account the previous conclusion and a mock model of the MAD-XR was installed onboard. The solution was to design and rapid prototype a wing pod, as shown in Figure 3.13.

(a) MSU mounted inside the pod

(b) N1 with wing tip pods installed

Figure 3.13: On the left, figure 3.13(a) shows a dimensional model of the MSU installed on the wing tip; On the right, figure 3.13(b) shows the N1 ready for take-off with the wing tip pods mounted

The final mass of the whole pod and MSU was 1.7kg, accounting for harnessing.

The flight testing represented on Figure 3.14 allowed to validate this concept, as the wing tip pods did not affect the overall performance of the aircraft. It also showed that the aircraft was capable to safely take-off and land without compromising the structural integrity of the MSU.

At this point, other obstacles came up, regarding the technical operation of the MAD-XR. Due to the high intensity of the magnetic field on the N1 wing tip, the sensor analysis could be influenced, supplying

Figure 3.14: N1 with pods mounted during flight testing

unreliable data, compromising the success of futures operations. Therefore, it was established the magnetic noise generated by the aircraft, and respective components on the sensor's location, should not be higher than 2nT, based on data from aircraft with similar operations [43].

Also, CAE alerted that due to performance and airworthiness issues, the cabling between MSU and MIU units required to be customized and to have a special type of connectors, which have a large thickness exceed, at some points, the wing geometry. This can be a problem for future purposes and maintenance issues, so it was recommended the whole system to fit in the wing.

These considerations were the basis for an optimization study of the wing, to obtain a new concept that accounts for all these new requirements and the ones set previously.

3.2 N1: Aerodynamics and Performance

Due to the fact only the wing should be modified to optimize the aircraft and increase the operation's overall efficiency, it was necessary to validate the aerodynamic model prior to the new wing conceptualization. From the data collected on previous flight testing on the N1, it was known the amount of power consumed on horizontal flight was approximately 600 W, when flying at 100m of altitude and with a speed of 24 m/s. Also, the N1 typically had a take-off weight of approximately 30kg and the power consumption accounts for 150W, to provide electric energy to the avionics. Having this in consideration, it was possible to set and refine the aerodynamic model, using several references, until the theoretical calculations matched the experimental results. Some technical data about the aircraft was not revealed due to intellectual properties from the owner company. Therefore, some assumptions regarding aircraft design process and physical measurements on the airplane were made to match, into the biggest extend possible, its characteristics.

3.2.1 Aerodynamic Characterization

The power supplied to the engine is computed based on the propulsive efficiency (η_{prop}) and the power required, which is the product of the flight velocity and the output thrust [44]. In horizontal flight, from Equation (3.4), $T = D$, which means, accounting for the 150W for avionics, the power supplied is given by

$$P_{sup} = \frac{V \times D}{\eta_{prop_e}{}^{a}} + 150 \tag{3.10}$$

The challenge now was to accurately model the aircraft drag so that the theoretical power consumption P_{sup} is approximately 600W, at the flight conditions specified before.

At this point during the project, a typical literature assumption on Equation (3.5) was made. It was assumed that the lift generated by the wing is substantially higher than the tail load P and, therefore, it is enough to match the aircraft's weight [41] [45] [46], $L \approx W$.

The lift load L and the drag D can be computed from the flight conditions (speed and altitude) and aircraft structure. The most common notation to compute this values is

$$L = \frac{1}{2}\rho_\infty S V^2 C_L \tag{3.11}$$

$$D = \frac{1}{2}\rho_\infty S V^2 C_D \tag{3.12}$$

where ρ_∞ is the air density at the flight altitude, S is the wing planform area and V is the flight speed. C_L and C_D are lift and drag coefficients, respectively, non-dimensional values that take into account the aircraft shape and the angle of attack α [44].

The lift coefficient is an adimensional value that quantifies the variations on the generation of the lift load when the aircraft angle of attack changes, as shown in Figure 3.15. The drag coefficient accounts

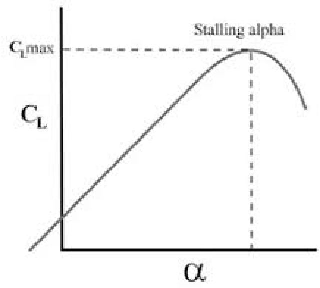

Figure 3.15: C_L vs α curve

for friction effects and disturbances on the flow. A more detailed explanation is required, in order to comprehend what causes drag in the aircraft. Anderson [44] states the total drag of an airplane can be divided into three major components, as shown in the next equation:

(Total Drag) = (Parasite Drag) + (Wave Drag) + (Induced Drag) (3.13)

Re-writing eq. 3.13 in terms of coefficients, it becomes

$$C_D = C_{D_0} + C_{D_w} + C_{D_i} \tag{3.14}$$

[a] According to flight data on electric mode: $\eta_{prop} = \eta_{propeller}\eta_{elecmotor}\eta_{losses} = 0.65$

3.2.1.a) Induced Drag: C_{D_i}

As explained in Section 3.1.2.a), the lift load is generated by the difference in the local pressure on the upper and lower wing. Close to the wing tips, the air is free to move from the region of high pressure into the low pressure, contouring the tip and generating a pair of counter-rotating vortices, one at each wing tip. This vortices produce a swirling flow of air downstream the wing which is very strong near the wing tips and decreases toward the wing root, as shown in Figure 3.16.

Figure 3.16: Wing Tip Vortices. Adapted from [47]

Depending on the atmospheric conditions, these phenomena can be observed on airliners' landing.

The induced flow on the vortices generates an additional downstream component of the aerodynamic force of the wing, that increases the drag.

The induced drag coefficient computation is based on 3D wing theory, and is deduced from wings that have an elliptical lift distribution [40]

$$C_{D_i} = \frac{C_L^2}{\pi AR} \tag{3.15}$$

where AR is the wing aspect ratio, given by $AR = \frac{S}{b}$, which, in this case, for the N1, is equal to 14.75.

This load distribution allows the wing to generate the less induced drag, when producing the same amount of lift as another wing, with a different distribution [40] [48]. However, there are few wings can actually have this characteristic, so Equation (3.15) is commonly described as

$$C_{D_i} = \frac{C_L^2}{\pi ARe} \tag{3.16}$$

where e is the Oswald's span efficiency factor, which accounts for extra drag due to separation drag and non-elliptical lift distribution. Typically, this value is assumed to be 0.8 [45][48].

C_L is computed rearranging Equation (3.11)

$$C_L = \frac{2L}{\rho_\infty SV^2} \tag{3.17}$$

Knowing $L = W$ and $V = 24$ m/s, is obtained $C_L = 0.806$, which gives $C_{D_i} = 0.0176$

3.2.1.b) Wave Drag: C_{D_w}

Some aircraft fly at velocities higher than the speed of sound, which can be deduced from the environmental thermodynamic[3] conditions, using the following equation [39]

$$a = \sqrt{kRT} \tag{3.18}$$

where k is the air specific heat ratio, R the gas constant for the air and T the absolute temperature, in Kelvin[4], $[K]$. The Mach number is the ratio between the flow velocity and the speed of sound [40]

$$M_a = \frac{V_\infty}{a_\infty} \tag{3.19}$$

When an aircraft is flying at velocities higher than the speed of sound, $M_a > 1$, the free-stream is at supersonic speeds, giving origin to large discontinuous property changes, also called shock waves [39]. These discontinuities cause a pressure pattern around the airplane which leads to a strong pressure asymmetry in the drag direction generating wave drag [44]. Typically, shock waves only occur if $M_a \geq 1$ but discontinuities of the environmental properties can happen at lower velocities, starting at $M_a = 0.8$ [39], which also produce wave drag

In this study, because the N1 flies at low subsonic speeds, the wave drag was C_{D_w} considered to be null.

3.2.1.c) Parasite Drag: C_{D_0}

This component is usually called *zero-lift drag*. If rearranging eq. (3.14) with the assumptions demonstrated previously, it is obtained

$$C_D = C_{D_0} + \cancelto{0}{C_{D_w}} + C_{D_i} = C_{D_0} + \frac{C_L^2}{\pi ARe} \tag{3.20}$$

Then, attending to Equation (3.11), if the $L = 0$, C_L is null, which means

$$C_D = C_{D_0} \tag{3.21}$$

To determine the total parasite drag coefficient, a *Component Build-up Method* [48] was used. This methods allows the estimation of the subsonic profile drag of each component of the aircraft: wing, tail, fuselage, etc.. It requires the computation of the skin-friction drag coefficient C_f, which is deduced assuming flat-plate equations [48] [44], an interference factor, the ratio of wetted and planform wing area and a component Form Factor $\mathcal{F}$, that estimates the pressure drag due to viscous flow separation [48].

Additionally, is necessary to account for leakages in the aircraft components, which create zones with different pressures in the aircraft that generate additional drag, and protuberances, such as external

[3] For further details, please consult [39] [49]

[4] $T(K) = 273.15 + T(^oC)$

devices such as antennas, control surfaces actuators, etc., which are noted as $C_{D_{LP}}$ [48]. Finally, there are unavoidable drag contributions that are not accounted for in the preceding formulations, which will be noted as $C_{D_{misc}}$ [50] [48].

The parasite drag build-up is shown in Equation 3.22

$$C_{D_0} = \sum \frac{C_{f_c}\mathcal{F}_c\mathcal{Q}_c S_{wet_c}}{S_{ref}} + C_{D_{misc}} + C_{D_{LP}} \tag{3.22}$$

The last two parameters are usually computed as a multiplication factor of the first parcel in Equation (3.22). According to [48], $C_{D_{LP}} \approx 10\% C_{D_{0_{tail}}}$ and $C_{D_{misc}}$ is approximately 5% of total parasite drag of the aircraft.

Regarding this type of drag, typical subsonic aircraft will have a large influence skin-friction in the quantification of parasite drag than any other source[48].

The Reynolds number is a non-dimensional value that physically measures the ratio between the inertial and viscous forces acting on a fluid [40], being given by

$$Re = \frac{\rho_\infty V_\infty x}{\mu_\infty} \tag{3.23}$$

where ρ_∞ is the density of the fluid, x is a characteristic length, V_∞ is the free-stream velocity, and μ_∞ is the dynamic viscosity. When contouring the wing, friction effects between the free-stream and the surface will have an impact on the behaviour of the flow, having consequences upon the generation of drag. The Reynolds number is important, because it allows the characterization of the flow around the wing and, therefore, to quantify these effects on the generation of drag.

Wing

The wing is a crucial component on aircraft design. Depending on the target mission profile and requirements, this structure is shaped differently, to achieve the best performance and stability. Figure 3.17 illustrates these characteristics

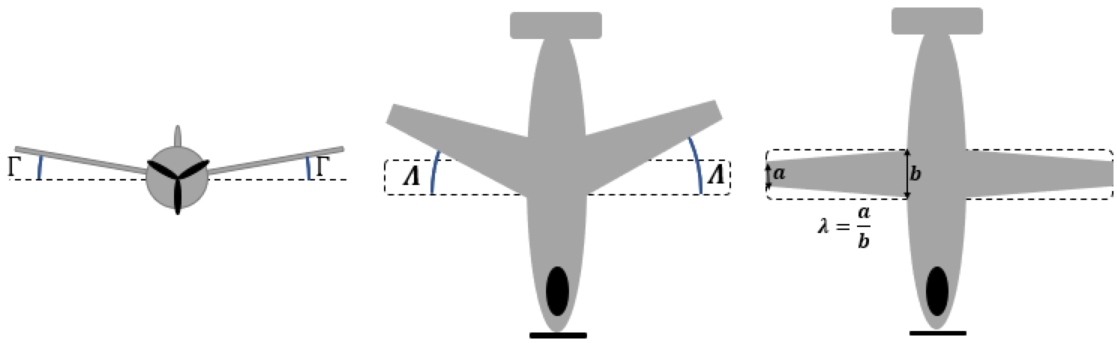

Figure 3.17: On left, there is a representation of wing with a positive dihedral, Γ. In the middle, there is a swept wing, with a sweep angle Λ. On the right, a tapered wing, in which the taper ratio λ is the ratio between the tip over the root chords

The N1 wing has no dihedral and is tapered. It was known the sweep angle has variation along the span, as shown in Figure 3.19. However, since technical data on this subject was not available, it was assumed the sweep angle Λ was null at the wing root.

The airfoil used on the N1's wing was not revealed so the aerodynamic characteristics were estimated from drawings and measurements of the wing, as shown in Figure 3.18, being summarised in Table 3.1

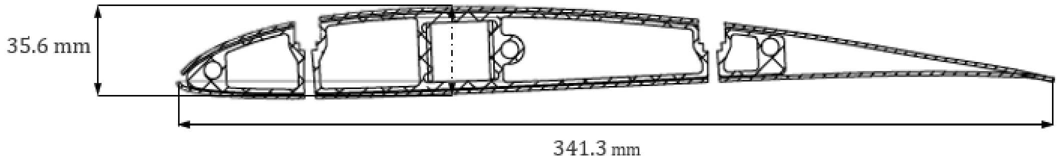

Figure 3.18: N1 Wing Section. Adapted from drawings

Figure 3.19: N1 Top view

Parameter	Value
$^t/_c$	0.105
$\left(^x/_c\right)_{t_{max}}$	0.33
$\Lambda\ [^o]$	0

Table 3.1: N1 wing aerodynamic parameters

The friction coefficient will vary with behaviour of the flow, when contouring the wing. For laminar flow, it is given by:

$$C_f = \frac{1.328}{\sqrt{Re_x}}, \tag{3.24}$$

On the other hand, for turbulent flow, the friction coefficient is computed by

$$C_f = \frac{0.455}{(\log_{10} Re_x)^{2.58}(1 + 0.144M_{eff}^2)^{0.65}} \tag{3.25}$$

where $M_{eff} = M_\infty \cos \Lambda_{LE}$. On swept wings is necessary to account for decreases in generation of lift due to a decrease in the effective dynamic pressure $q_{eff} = \frac{1}{2}\rho V_0^2 \times \cos \Lambda_{LE}$.

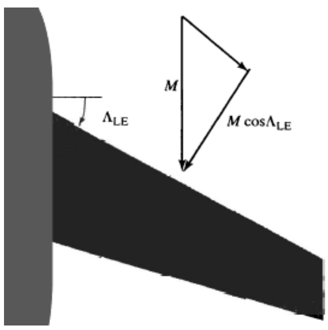

Figure 3.20: Effects of sweep angle on the effective parameters [45]

In this case, $M_{eff} = M_{V_0}$ because $\Lambda_{LE} = 0$.

The Reynolds number must be computed accordingly with the flight conditions. Because the N1's altitude during flight testing was low, it assumed sea-level conditions for the environmental parameters [39]:

Property	Value
$\rho\,[kg/m^3]$	1.225
$\mu\,[kms/m^2]$	1.81×10^-5
$\nu\,[m^2/s]$	1.50×10^-5

Table 3.2: Air properties at sea level

Making an approximation to the Reynolds number at the mean aerodynamic chord, $\overline{c}$, and defining $V_0 = 24$ m/s, the value obtained was computed as follow:

$$Re_{\overline{c}} = \frac{V_0 \overline{c}}{\nu} = \frac{24 \times 0.265}{1.460 \times 10^-5} = 3.29 \times 10^6 \tag{3.26}$$

For conventional airplanes in subsonic flight, it is reasonable to assume the flow is completely turbulent, as transition occurs near the leading edge [44]. The location of this phenomena can be estimated using the Reynolds number [44]

$$3.5 \times 10^5 \leqslant Re_{transition} \leqslant 1 \times 10^6 \tag{3.27}$$

Corke [45] states $\sqrt{Re} \geqslant 1000$, the flow is considered turbulent, which supports Equation 3.27.

Therefore, $Re_{\overline{c}} = 3.29 \times 10^6 \geqslant 1 \times 10^6$, which means the follow around the N1 wing can be assumed as turbulent, and Equation 3.25 was used to compute the skin-friction drag coefficient.

$$C_{f_{wing}} = \frac{0.455}{(\log_{10} Re_{\overline{c}})^{2.58}(1 + 0.144 M_{V_0}^2)^{0.65}} = 0.0036 \tag{3.28}$$

The form factor $\mathcal{F}$ estimates the increase in friction coefficient due to flow separations. For lifting surfaces, such as wing [45], tail and canards [48], it is given by

$$\mathcal{F} = \left[1 + \frac{0.6}{\left({}^{x}\!/_{c}\right)_{t_{max}}}\left(\frac{t}{c}\right) + 100\left(\frac{t}{c}\right)^4\right]\left[1.34 M^{0.18}(cos(\Lambda_{t/c_{max}}))^{0.28}\right] \tag{3.29}$$

where t/c_{max} and $\left({}^{x}\!/_{c}\right)_{t_{max}}$ are properties from the airfoil, previously defined on table 3.1. $\Lambda_{t/c_{max}}$ is the sweep angle at the maximum thickness line.

Making the approximation $\Lambda = 0$ over the chord, Equation 3.29 is reduced to

$$\mathcal{F} = \left[1 + \frac{0.6}{\left({}^{x}\!/_{c}\right)_{t_{max}}}\left(\frac{t}{c}\right) + 100\left(\frac{t}{c}\right)^4\right]\left[1.34 M_{V_0}^{0.18}\right] \tag{3.30}$$

where, after substitution of the values in table 3.1, $\mathcal{F}_{wing} = 1.002$.

Due to the fact the N1 is a high-wing aircraft, the interference is assumed to be negligible [48], so the factor $\mathcal{Q}$ is equal to 1 [48][45].

Finally, it was necessary to quantify the wing's wetted area, which is the actual surface of material that is in contact with the flow, where friction occurs [44]. According to [45], it can be approximated by a function that depends on the wing's maximum thickness-to-chord ratio $(t/c)_{max}$:

$$S_{wet} \simeq \begin{cases} 2.003S & \text{if } (t/c)_{max} \leqslant 0.05 \\ (1.977 + 0.52\,(t/c)_{max})S & \text{if } (t/c)_{max} > 0.05 \end{cases} \tag{3.31}$$

where S is the wing planform area.

Because the thickness-to-chord ratio is higher than 0.05, the second equation was used, obtaining $S_{wet} = 2.032S$.

Fuselage

With the dimensions of the fuselage set, the calculations regarding the parasitic drag coefficient introduced by skin friction, C_{D0}, can now be performed using the following expression [45]:

$$C_{D0} = \frac{F_f + F_w}{qS} \tag{3.32}$$

Where S is the wing area and F_f is the friction drag, given by:

$$F_f = qS_{wet}C_f\mathcal{F}\mathcal{Q} \tag{3.33}$$

F_w represents the wave drag which, in this case, is not considered once the flight is subsonic. Taking this into account and substituting Equation 3.33 on 3.32, the following equation is obtained

$$C_{D0} = \frac{qS_{wet}C_f\mathcal{F}\mathcal{Q}}{qS} = \frac{S_{wet}C_f\mathcal{F}\mathcal{Q}}{S} \tag{3.34}$$

Here, S_{wet} is the wetted area of the fuselage, C_f is the friction drag coefficient of a flat plate, $\mathcal{Q} \approx 1$ is the interference factor and $\mathcal{F}$ is the form factor, which can be written as [45] [48]

$$\mathcal{F} = 1 + \frac{60}{f^3} + \frac{f}{400} \tag{3.35}$$

where f is the fuselage's fineness ratio between the maximum diameter and the length: $f = \left(\frac{l_f}{d_f}\right)$

Note that Equation 3.34 defines C_{D_0} similarly to Equation 3.22, when applied to the fuselage, so the approach from [45] is in agreement with the one took from [48]. According to [48], using graphical integration on the fuselage cross-sections is a very accurate method to compute this parameter, as shown in Figure 3.21(a). However, neither drawings or computational models were available on this stage of the project. Another method from the same author, is to measure the fuselage's area from top and side views (Figure 3.21(b)). Then, the values are averaged and multiplied by a factor that depends on the body's cross section, perpendicular to the longitudinal axis of the aircraft. For most airplanes, a factor equal to 3.4 provides a reasonable approximation:

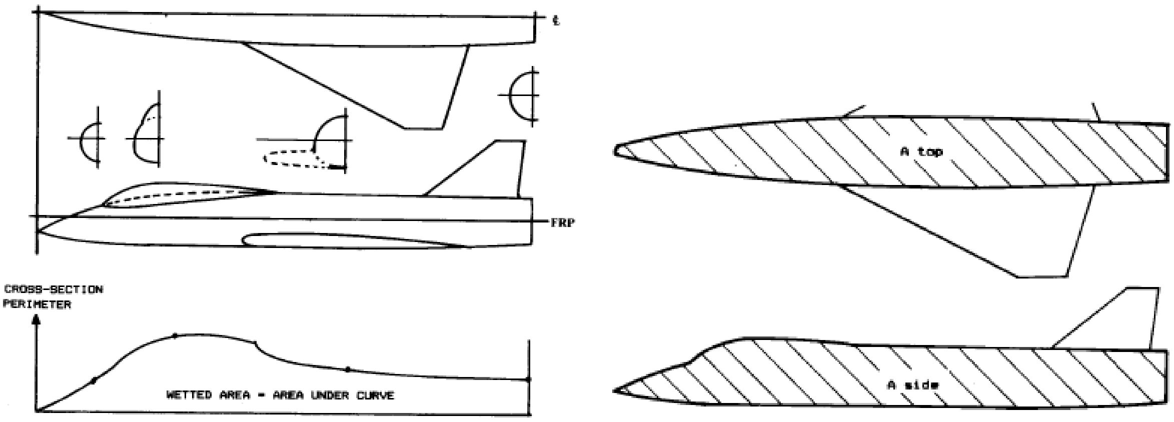

(a) Perimeter calculation for numerical methods

(b) Projected Areas

Figure 3.21: On the left, figure 3.21(a) shows a numerical integration method; On the right, figure 3.21(b) makes the computation of the area from top and side views of the aircraft[48].

$$S_{wet} = 3.4\frac{A_{top} + A_{side}}{2} \tag{3.36}$$

However, initial computations using this method were not concordant with the objective reference, discussed in the begin of this section. Therefore a theoretical approximation of the fuselage wetted area was made, based on a quantitative shape described in [45]. This allows the computation of the total wetted area as well as the friction coefficient, which varies according to the flow regime (laminar or turbulent), as mentioned in the wing section.

For the estimation of the value of S_{wet}, the fuselage shape was divided into 100 piecewise-linear x-portions with constant dimensions:

$$S_{wet} = \sum_{1}^{100} P_i x_i \tag{3.37}$$

The problem now consists in the determination of the P_i coefficients which represent the perimeter of the fuselage at a given point, x_i. To do so, there was the need to calculate the radius of the fuselage at any x_i which, according to [45], can be performed using one of various theoretical approximations.

The Sears-Hacks approximation considers the fuselage as a symmetric body of revolution. Here, the profile can be described by the following ratio:

$$\left[\frac{r(x)}{r(0)}\right]^2 = \left[1 - \left(\frac{2x}{l}\right)^2\right]^{\frac{3}{2}} \tag{3.38}$$

Where:

$r(x)$ is the radius of the considered fuselage at any point $\frac{-l}{2} \leq x \leq \frac{-l}{2}$ of the fuselage

$r(0)$ is the maximum radius of the fuselage, $\frac{d_f}{2} \approx 0.15$m

l is the overall length, $l_f = 2$m, estimated in the previous subsection

The total area calculated using this approximation was $S_{wet} = 1.39$m^2 leading to $C_{D0} \approx 0.0046$.

Tail

The last group to be evaluated is the tail, which is decomposed in the vertical and horizontal components. Similar to the wing, no data regarding the tail aerodynamics was available. Therefore, a 4-digit NACA airfoil was assumed for the approximation. Taking measurements from the aircraft and knowing these are usually symmetric, a NACA 0009 was used.

However, some considerations about the tail geometry must be considered.

Parameter	Value
Planform Area m^2	0.158 [b]
MAC m	0.171 [b]
$^t/_c$	0.09[c]
$\left(^x/_c\right)_{t_{max}}$	0.31[c]
Λ $[^o]$	0[b]

Table 3.3: Horizontal Tail

Parameter	Value
Planform Area m^2	0.06[c]
MAC m	0.17[c]
$^t/_c$	0.09[b]
$\left(^x/_c\right)_{t_{max}}$	0.31[b]
Λ $[^o]$	35[c]

Table 3.4: Vertical Tail

The process to estimate the base drag of the horizontal tail is similar to the wing, due to the similarity on the sweep angle, $\Lambda_{ht} \approx 0^o$. However, for the vertical tail, it is necessary to account for changes in the effective properties, due to $\Lambda_{vt} = 35^o$.

3.2.1.d) Drag Build Up

The following table summarizes the parasite drag of each component

Parameter	Wing	Fuselage	Vertical Tail	Horizontal Tail
C_f	0.002	0.0042	0.0026	0.0025
Q	1	1	1.05	1.05
F	1.002	1.22	0.953	0.985
S_{wet}/S	2.032	1.39	0.117	0.32
C_{D_0}	**0.0041**	**0.0069**	**0.0003**	**0.0008**

Using the entries of the previous table on Equation (3.22), it is possible to obtain the aircraft parasite drag

$$C_{D_0} = \left(\sum \frac{C_{f_c} \mathcal{F}_c \mathcal{Q}_c S_{wet_c}}{S_{ref}} + 0.1 C_{D_{0_{tail}}} \right) \times 1.05 = 0.0129 \tag{3.39}$$

[b]Obtained from NACA 0019 analysis using XFLR5.
[c]Obtained from measurements on the aircraft and drawings.

which is used on Equation (3.20) to compute the total drag coefficient

$$C_D = 0.0129 + 0.0176 = 0.0304 \tag{3.40}$$

With this result, using Equation (3.10), the total supplied from the engine is

$$P_{sup} = \frac{V_0 \times \frac{1}{2}\rho S V_0^2 C_D}{\eta_{prop_e}} + 150 = 565W \tag{3.41}$$

Since the target value from flight experience was 600W, the obtained result has an error of 5.8%. The difference between these two values is justified by the fact the N1 has already gone through a series of optimizations and re-tuning while this characterization has its fundamentals on preliminary aircraft design. It also required several assumptions for parameters that were not revealed due to intellectual property rights, which decrease the accuracy when comparing to experimental flight results. Also, complex aerodynamic phenomena, such as trimming drag from the tail, required longer computation effort that was not necessary at this stage.

Due to the project's conceptual nature, this approximation was considered valid and used into the next stages, where the aircraft's performance with the gas engine is analysed.

3.2.2 Operational Performance

Having an approximation on the aircraft aerodynamics, it was possible to estimate the N1 performance on the proposed operation with the aircraft in its base geometry.

When configured to fly with the electric engine, the N1 cannot meet the endurance requirements, so the gas engine configuration was chosen to fulfil the project' objectives. Therefore, a short study on the performance was carried out to evaluate the benefits of the main modifications of the aircraft.

Before, it is necessary to note that operation requires a VTOL capability, which still needs to be installed in the aircraft. Not having data about previous flight tests, it was assumed to aircraft would fly on its maximum capacity, with 35kg of take-off weight.

Also, it is important to highlight that the aerodynamic influence of the VTOL mounting and motors were not accounted in this study, due to complex aerodynamic phenomena, that would require the use of wind-tunnel testing or Computational Fluid Dynamics (CFD) analysis.

Therefore the aircraft flight qualities were estimate using Corke's methodology [45],

3.2.2.a) Propulsion Validation

Since any detailed data on the combustion engine efficiency was available, a theoretical approximation was made, based on previous flight testing. According to the N1's designer [34], the N1 is able to fly approximately 3 hours per kilogram of fuel, when flying at 24m/s. Therefore, using the Breguet Equation for endurance [45], is obtained:

$$E = \frac{\eta_{prop_g} \times L/D}{TSFC \times g \times V_0} \ln\left(\frac{W_i}{W_f}\right) \tag{3.42}$$

Where η_{prop} is the overall propulsive efficiency, accounting for propeller, engine and transmission losses, and L/D is the lift over drag ratio. As for $TSFC$ it is used the value from the gas engine datasheet. E is the endurance flight time in hours, g is the gravitational acceleration at sea-level and W_i and W_f are the aircraft mass, in the initial and final point of the stage in study, respectively.

From [45]:

$$\frac{L}{D} = \frac{C_L}{C_D} \tag{3.43}$$

which means the lift to drag ratio is equal to ratio of the respective coefficients. Taking the values from Equations (3.17) and (3.40):

$$\frac{L}{D} = 26.87 \tag{3.44}$$

Parameter	Value
$TSFC\ \left[{}^{kg}/_{Whr}\right]$	6.3×10^{-4}
$E\ [hr]$	3
$V_0\ [m/s]$	24
$g\ \left[m/s^2\right]$	9.81

Table 3.5: Flight Testing parameters

The propulsive efficiency can be deduced rearranging Equation (3.42) as follows

$$\eta_{prop_g} = \frac{E \times TSFC \times g \times V_0}{L/D \times \ln\left(\frac{W_i}{W_f}\right)} \tag{3.45}$$

which gives an estimate of 49.1% for the propulsive efficiency of the combustion engine.

3.2.2.b) Fuel Assessment

In order to estimate the fuel weight, the flight was split into several segments according to the defined mission profile.

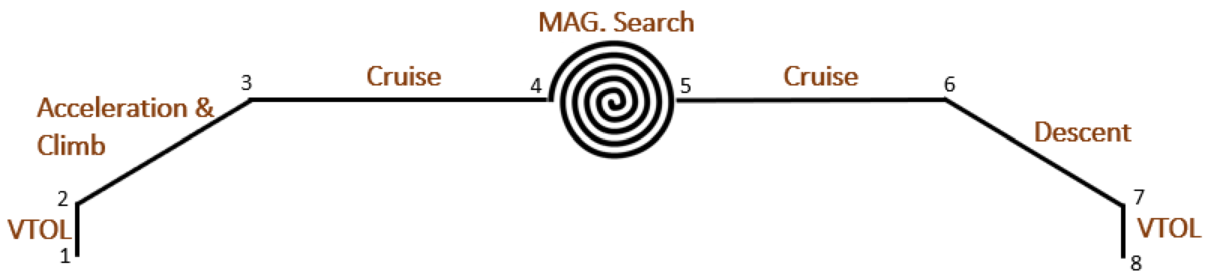

Figure 3.22: Mission profile

In this case, only the segments when the engine is providing thrust will be taken in consideration:

1. Acceleration & Climb: stage after Take-off, characterized by an increase of the aircraft speed and altitude until reaching cruise conditions;

2. Cruise/Dash:

3. Search/Patrol: with principles similar to loitering, in this stage is required to the aircraft to cruise for a specified amount of time over a specific region;

4. Dash Back:

5. Descent

Take-off and Landing were not considered because they will be performed using electric engines. It is assumed the mass of the batteries does not vary in these stages, which means the mass of the aircraft will be constant.

For each segment the fraction of final to initial weight W_f/W_i is computed giving the final weight loss as:

$$\frac{W_N}{W_0} = \frac{W_1}{W_0} \times \frac{W_2}{W_1} \times ... \times \frac{W_N}{W_{N-1}} \tag{3.46}$$

For N mission segments. Then, the total fuel weight can be estimated as:

$$W_{fuel} = W_{TO}\left(1 - \frac{W_N}{W_0}\right)(1 + ReserveFuel + TrappedFuel) \tag{3.47}$$

Where $ReserveFuel$ and $TrappedFuel$ are given in percentage and were assumed as 5% and 1%, respectively, as they represent standard values provided in literature [45].

Acceleration and Climb

For subsonic flight this value is given by

$$\frac{W_f}{W_i} = 1 - 0.04M_{a_{cr}} \tag{3.48}$$

where $M_{a_{cr}}$ is the Mach number in cruise.

As described in section 3.48, the required cruise speed, V_{cr}, is 50 m/s. Because sea-level conditions are assumed, the sound speed,a, is equal to 340 m/s. Therefore,

$$M_{cr} = \frac{V_{cr}}{a} = \frac{50}{340} = 0.14 \tag{3.49}$$

Applying this value on Equation (3.48)

$$\frac{W_3}{W_2} = 1 - 0.04 \times 0.14 = 0.994. \tag{3.50}$$

Dash

For this stage the Breguet equation for propeller-driven aircraft is used, given as

$$\frac{W_f}{W_i} = \exp\left(-\frac{TSFC \times g \times R}{\eta_{prop} \times L/D}\right) \tag{3.51}$$

Where R corresponds to the distance the aircraft must cover.

Parameter	Value
$TSFC\ \left[{}^{kg}/_{Whr}\right]$	4.5×10^{-4}[d]
$R\ [m]$	37 040[e]
$g\ \left[m/s^2\right]$	9.81
η_{prop_g}	0.491

Table 3.6: Cruise segment parameters

From Equation 3.43:

$$\frac{L}{D} = \frac{C_L}{C_D} \tag{3.52}$$

Therefore:

$$C_L = \frac{2 \times W_3 \times g}{\rho_\infty \times V_{cr}^2 \times S} = 0.215 \tag{3.53}$$

where W_3 is the aircraft in the beginning of cruise stage.

The drag coefficient's calculation, C_D, required the use of the aerodynamic model described earlier because the environmental conditions differ, which has implications for parasite drag, C_{D_0}.

Using Equation (3.20)

$$C_D = C_{D_0} + kC_L^2 = 0.0117 + 0.027 \times 0.215^2 = 0.013 \tag{3.54}$$

where $k = \frac{1}{\pi ARe} = 0.027$.

Applying these results to Equation (3.43)

$$\frac{C_L}{C_D} = \frac{0.215}{0.013} = 15.97 \tag{3.55}$$

With all parameters defined, after substitution on Equation (3.51) and dimensional verification, the fuel fraction for the first cruise stage was computed as follow

$$\frac{W_4}{W_3} = \exp\left(-\frac{\left(4.5 \times 10^{-4}\right) \times 9.81 \times 37040}{3600 \times 0.491 \times 15.97}\right) = 0.994 \tag{3.56}$$

Before continuing the process, there are a few topics to discuss:

1. The L/D ratio is small when compared to aircraft similar to the N1. Usually, this value is around 25 for airplanes with those characteristics. It is important to note that the cruise speed typically corresponds to the maximum lift-to-drag ratio [45]. If the speed increases beyond this value, is common to verify a decrease on the L/D[44]. In this case, it has been consider a speed of 50 m/s, when the N1 cruise speed is 26 m/s, reason why this ratio is low.

2. Upon the estimation of L/D ratio, is important to account for variations on the $Lift$ load, due to the decrease of the fuel's mass [45]. However, because the weight fraction $\frac{W_4}{W_3} \approx 1$, this variation was neglected.

[d]Based on engine datasheet
[e]20nm=20$\times$ 1 853 m

Patrol/Search

As said before, on this stage is required the aircraft to fly for a specific amount of time, at a determined speed. To estimate the weight fraction it, the Breguet endurance equation is used, which after rearrangements, is given by

$$\frac{W_f}{W_i} = \exp\left(-\frac{TSFC \times g \times E \times V_{ltr}}{\eta_{prop_g} \times L/D}\right) \tag{3.57}$$

Most of parameters are the same from the cruise, except for the endurance time, E, replacing the range to cover R, and the flight speed, V_{ltr}.

Parameter	Value
$TSFC\ \left[{}^{kg}/_{Whr}\right]$	4.5×10^{-4}
$E\ [hr]$	8
$V_{ltr}\ [m/s]$	40
η_{prop_g}	0.491

Table 3.7: Patrol segment parameters

Despite the values of $TSFC$ and η_{prop} change with the mission stage and with the external flow speed, respectively, they were kept equal on cruise and loiter, for simplicity on the computation.

To estimate the L/D, an iterative process was conducted because the mission's highest fuel consumption occurs in this stage. First, the aircraft mass at the begin of the segment is computed:

$$W_4 = W_{TO} \times \frac{W_4}{W_3} \times \frac{W_3}{W_2} \tag{3.58}$$

where W_{TO} is the take-off weight, in kilograms. Note that $\frac{W_2}{W_1}$ is not considered in Equation (3.58) because it is assumed the aircraft remains constant, when using the VTOL electrical engines.

$$W_4 = 35 \times 0.994 \times 0.994 = 34.59 \text{ kg} \tag{3.59}$$

The next step is to compute the lift-to-drag ratio, the same way as the previous segment. Rearranging Equation (3.43) with respect to Equation (3.20):

$$\frac{C_L}{C_D} = \frac{C_L}{C_{D_0} + kC_L^2} \tag{3.60}$$

From the aerodynamic model:

$$\left(\frac{C_L}{C_D}\right)_4 = \frac{0.335}{0.012 + k0.335^2} = 22.27 \tag{3.61}$$

Then, when all the parameters are defined, the first estimation of the fuel fraction is computed. Note that :

$$\left(\frac{W_5}{W_4}\right)_1 = \exp\left(-\frac{\left(4.5 \times 10^{-4}\right) \times 9.81 \times 8 \times 40}{0.491 \times 22.27}\right) = 0.879 \tag{3.62}$$

Finally, the lift-to-drag ratio in the end of the segment is calculated, attending the decrease in the fuel's mass and assuming all environmental and performance conditions kept constant.

$$W_5 = \frac{W_5}{W_4} \times W_4 = 34.59 \times 0.879 = 30.39 \text{ kg} \tag{3.63}$$

which implies $C_{L_5} = 0.294$, attending to Equation (3.17)

To account for degradations on the lift-to-drag ratio, a linear average of the C_L during this segment is made, assuming that every external condition remains constant. Therefore,

$$C_{L_{ltr}} = \frac{C_{L_4} + C_{L_5}}{2} = 0.314 \tag{3.64}$$

which gives the average L/D of this segment

$$\left(\frac{C_L}{C_D}\right)_{ltr} = \frac{0.314}{0.015 + k0.314^2} = 21.39 \tag{3.65}$$

Finally, recomputing the fuel fraction with the averaged L/D:

$$\left(\frac{W_5}{W_4}\right)_2 = \exp\left(-\frac{\left(4.5 \times 10^{-4}\right) \times 9.81 \times 8 \times 40}{0.491 \times 21.39}\right) = 0.874 \tag{3.66}$$

Repeating this process for n-iterations until $\left({}^{W_5}/{}_{W_4}\right)_n - \left({}^{W_5}/{}_{W_4}\right)_{n-1} = 0$, would allow a precise estimate of this approximation. However, because $\left|\left({}^{W_5}/{}_{W_4}\right)_2 - \left({}^{W_5}/{}_{W_4}\right)_1 < 0.01\right|$, it was considered the results had converged.

Similar to dash segment, there some aspects that are not in agreement with typical practices in aircraft performance. For common propeller-driven airplanes, is usual the $\left(L/D\right)_{cr} > \left(L/D\right)_{ltr}$ [48]. This condition does not verify in this study because the required loiter speed is closer to the to the design optimum speed of the aircraft, when compared to results from the previous stage.

Return Dash

Equal to segment (3-4), except the changes in the aircraft mass must be accounted. The same conditions also apply in this segment, from the previous computation it is known the L/D is given by

$$\left(\frac{C_L}{C_D}\right)_6 = \frac{0.187}{0.012 + k0.187^2} = 14.45 \tag{3.67}$$

which means a fuel fraction of

$$\frac{W_6}{W_5} = \exp\left(-\frac{\left(4.5 \times 10^{-4}\right) \times 9.81 \times 37040}{3600 \times 0.491 \times 14.45}\right) = 0.994 \tag{3.68}$$

Descent

In this stage, is common to assume the aircraft is flying idly (no fuel is consumed) or to consider the distance covered on this stage is part of aircraft's range [45]. Therefore, the fuel fraction is considered to be equal to 1.

Total fuel

Flight Segment	Value
Acceleration & Climb (2-3)	0.994
Dash (3-4)	0.994
Patrol/Search (4-5)	0.874
Return Dash (5-6)	0.994
Descent (6-7)	1

Table 3.8: Fuel Fraction

The following table summarises the fuel fraction for each segment:

Having all segments computed, using Equation (3.46)

$$\frac{W_f}{W_{TO}} = \frac{W_3}{W_2} \times \frac{W_4}{W_3} \times \frac{W_5}{W_4} \times \frac{W_6}{W_5} \times \cancelto{1}{\frac{W_7}{W_6}} = 0.859 \tag{3.69}$$

Finally, substituting this value on Equation (3.47), is possible to estimate the mass of fuel required for the N1 to fulfil this mission:

$$W_{fuel} = W_{TO} \left(1 - \frac{W_f}{W_{TO}}\right) (1 + 0.05 + 0.01) = 5.24 \text{ kg} \tag{3.70}$$

3.2.2.c) Performance Summary

It is important to highlight the fact this study **did not** account the wingtip pods that carry the MAD-XR's MSU and respective counter-weight. During flight, their presence will reflect an increase on the overall wetted area, which increases the aircraft parasite drag, C_{D_0}, and, by its term, the fuel consumption. This subject will be discussed in more detail in Chapter 4

However, there is a benefit. Having wingtip pods will reduce the effects of vortex generation on the wingtip, which will reduce the lift-induced drag [42]. This matter, due to its complexity, was not studied during this project.

4

Wing Modification: Design, Optimization and Analysis

Contents

4.1 Parametric Optimization

4.1.1 Problem Contextualization

The first step when doing an optimization is to understand the problem, the objective, the design variables and constraints.

The problem's objective function is a function that the optimizer analyses with the main goal of finding its minimum. The design variables are the parameters the user is looking for to find its solution. The constraints are boundaries to the solution. For example, consider the following optimization problem:

$$\begin{array}{rl} \text{minimize} & f(x) = x_1 + x_2 \\ \text{by varing} & x \in R^2 \\ \text{subject to} & g(x) = x_1^2 + x_2^2 \leq 4 \end{array}$$

This problem had a constraint, $g(x)$, and the goal was to find the minimum of $f(x)$, regarding $g(x)$.

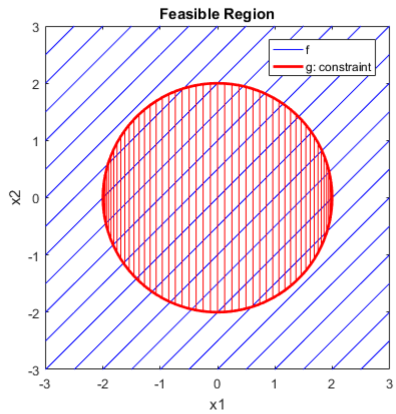

Figure 4.1: Plot of f regarding g

In the case of this simple problem, the solution can be to visualized in a 2D plot. In Figure 4.1, is shown, in blue, the objective function $f(x)$ and, in red, the constraints $g(x)$. The problem is to find the minimum value of f that respects the constraint function g, by varying $x = (x_1, x_2)$. In simple words, is to find the combination with minimum value of f that is "inside" the red circle.

Observing the plot, and making some calculus, it is possible to conclude that the minimum value of (x_1, x_2) is $(-\sqrt{2}, -\sqrt{2})$.

Regarding the constraint, note that $g(x)$ is set to be less or equal to 4. This means that if $g(x) = 4$, the solution is valid. This is a case where a the constraint is also a solution for the problem, and is called "active constraint". If there was no equality on the constraint function, it would be called "inactive constraint" [51].

Again, on Figure 4.1 it is also possible to define the problem's feasible region, which basically is the set of variables that actually constitutes a solution for the problem. In this case, is the domain inside the red circle.

Not every optimization problem is like this. In fact, most of them do not have a physical representation due the inherent level of complexity. There are several methods and algorithms of optimization and is up to the user to choose the most convenient to solve its problem, since there are no mandatory rules of when applying one method or other [51].

In this case, it was chosen to perform a parametric optimization, due to the fact that most design variables were known and the problem was already defined in almost all variants. Also, this method does not require long implementation effort and has the benefit of being compatible with the aerodynamic model implemented earlier on Chapter 3.

4.1.1.a) Aircraft Design

The intent is to modify the aircraft as minimum as possible. The wing, because it is the structure housing the sensor, is the only object of study in this project. It is assumed all other components, such as tail and fuselage, will remain as they were in the initial configuration.

Then, there were three main design variables, in which two were directly affected from the requirements:

t thickness, given the large size on wiring connectors;

b wing span, to decrease the amount of magnetic noise generated by the VTOL engines;

The last variable is the wing area, S, and it was chosen due to its large influence on the aircraft generation of both lift and drag.

The goal of this optimization is to compute the wing parameters that will minimize the mass of fuel consumed, which is directly influenced by the amount of drag the aircraft needs to overcome.

Thickness, t

From the MAD-XR manufacturer on Section 2.2.3, the sensor cabling has a large connector, which diameter is approximately 2.5cm. Therefore, it was established that 3.5cm would be the minimum thickness of the wing, to allow all the cabling to pass through its cross-section. Also, from the aircraft designer experience, this thickness would also give the wing enough stiffness to endure the aerodynamic loads.

At this point, it was assumed that the thickness-to-chord ratio was going to be uniform along the wing. Knowing that its planform is defined to have a variable chord, it is necessary to guarantee a minimum $t_{tip} = 0.035m$ to match the design requirements. Therefore, the thickness-to-chord ratio was set as a design variable.

Wing Span, b

Hansen's magnetic characterization of the N1 [8] estimated the intensity of the magnetic field all over the aircraft. Having a minimum value of this parameter in the MSU's location required an assessment of the distance this device should be from the VTOL engines. In other words, it required to know the variation of the magnetic field at the wing tip when the wing span varies. To avoid having to evaluate the magnetic field intensity on every iteration, a surrogate model of the variation of the magnetic field along the wing span was developed, based on his model.

This allowed to have an approximation function of the magnetic field intensity, based on theoretical data

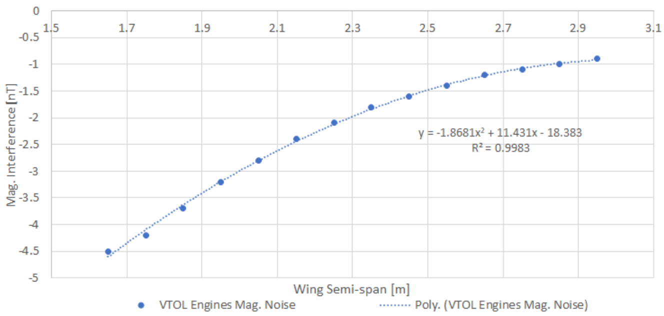

Figure 4.2: Determination of the magnetic field approximation function

The approximation function that quantifies the amount of magnetic noise at the wing tip is given by:

$$B_{wingtip} = -1.8681(b/2)^2 + 11.431(b/2) - 18.383 \tag{4.1}$$

where b is the wing span.

This function constitutes a valid approximation due to the fact R^2 is close to 1.

With this, it was possible to find a minimum value that would meet the requirement of having a magnetic intensity lower than 2nT. Therefore,

$$B_{wingtip} = -1.8681(b/2)^2 + 11.431(b/2) - 18.383 = 2 \tag{4.2}$$

which, because it is a second-degree polynomial, has two solutions: 2.29 and 3.82. The second value was disregarded because the intent was to compute the minimum wing span that verifies the condition on Equation (4.2).

For simplification, a minimum of 2.3m was chosen for the wing span upon the optimization, whilst the maximum was already define as 2.45m, on section 2.2.3, due to cabling issues between MSU and MIU components of the MAD-XR.

Wing Area, S

The wing area was the only parameter that did not have a specific requirement from the entities involved in the project. However, when modifying an aircraft's wing, the final result shows different characteristics and capabilities. Therefore, to define the range of values for this parameter, a methodology similar to aircraft design project was carried [45], with the selection of the wing loading (W/S) and the power-to-weight ratio (P/W). The wing loading or the weight-to-wing area ratio is defined as the ratio of the gross weight of the aircraft to the planform area of main wing. The power-to-weight ratio is defined as the ratio of power necessary for each phase of flight plan to the gross weight of the aircraft. The wing loading and the power-to-weight ratio are selected by considering the aircraft mission and its principle requirements, which include the following [45]:

- Stall speed
- Cruise speed
- Take-off distance
- Climb rate
- Acceleration to cruise Mach
- Instantaneous turn rate
- Descent rate
- Maximum ceiling
- Sustained turn
- Landing distance
- Range
- Endurance

From all the possible parameters shown previously, only the relevant ones for the intended aircraft (propeller-driven) and its operation were considered, as shown in the paragraphs that follow.

1. Cruise Speed

$$\frac{P}{W} \geq \frac{1}{\eta_p}\left[\frac{\rho_C V_C^3 C_{D_{0_C}}}{2\frac{W}{S}} + \frac{2k}{\rho_C V_{cr}}\frac{W}{S}\right] \tag{4.3}$$

Where:

ρ_{cr} is the air density at the cruise altitude. In this case, due to its low value (300ft), sea-level conditions were assumed for simplicity;

V_{cr} is the cruise velocity of 50 m/s, as required;

$C_{D_{0_{cr}}}$ is the drag coefficient at cruise speed. This value should be in the interval $[0.01; 0.02]$, with a value of 0.02 being chosen;

η_p is the propulsive efficiency at cruise conditions, with a value of 0.64;

2. Stall Speed

$$\frac{W}{S} \leq \frac{\rho_{TO} V_S^2}{2} C_{L_{max}} \tag{4.4}$$

Where:

ρ_{TO} is the air density at the considered take-off altitude, in this case, sea-level;

V_S is the stall velocity, set at 20 m/s from previous configuration;

$C_{L_{max}}$ is the maximum lift coefficient. Because there are no flaps, a value of 1.35 was chosen, from flight experimental data.

3. Range

$$\frac{W}{S} = \frac{\rho_{cr} V_{cr}^2}{2}\sqrt{\frac{C_{D_{0_{cr}}}}{k}} \tag{4.5}$$

Where:

ρ_{cr} is the air density at cruise altitude, which, in this case, is considered sea-level;

V_{cr} is the cruise of 200 kts. This value is one of the requirements;

$C_{D_{0_{cr}}}$ is the drag coefficient at cruise. From the method previously described, a value of 0.013 was chosen;

4. Endurance

$$\frac{W}{S} = \frac{\rho_{ltr} V_{ltr}^2}{2} \sqrt{\frac{3 C_{D_{0_{ltr}}}}{k}} \tag{4.6}$$

Where:

ρ_{ltr} is the air density at patrol altitude, which, in this case, is considered sea-level;

V_{ltr} is the patrol speed of 40 m/s;

$C_{D_{0_{ltr}}}$ is the drag coefficient at loiter/patrol segment. From the method previously described, a value of 0.015 was chosen;

After selecting the relevant constraints to the design, the expressions are plotted in a W/S to P/W axis. From this graph a design point can be chosen as long as it is contained in the admissible area that complies with all the criteria. In figure 4.3 the plot generated is shown.

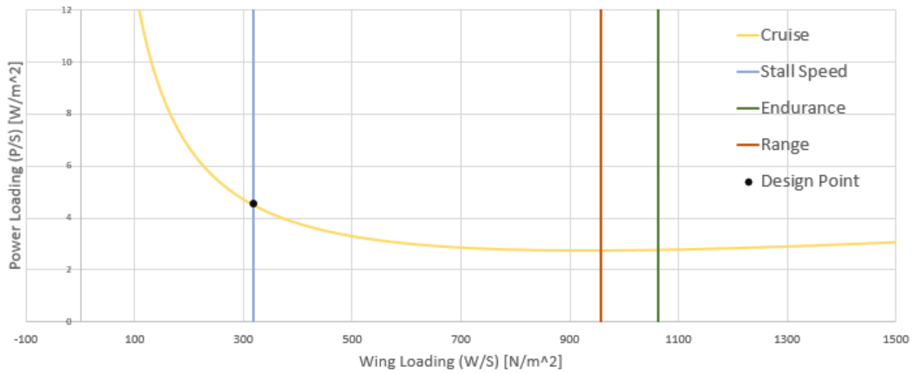

Figure 4.3: Design Point

From the observation of figure 4.3 it is clear that the design point was chosen at the intersection of the stall speed and cruise constraints.

At this point, the power loading P/S is 4.52 W/m^2 and the wing loading W/S is 318.5 N/m^2. The latter allowed to obtain the minimum value for the reference area, which, in this study, is assumed to be the wing area

$$S_{wing_{min}} = \frac{W}{W/S} = \frac{35 \times 9.81}{318.5} = 1.07 m^2 \tag{4.7}$$

4.1.1.b) Aerodynamics

To compute the aerodynamic characteristics on the optimizer, the model discussed on Chapter 3 was used, with the addition of the wing tip pods or the MSU. Once again, the methodology suggested by Corke [45] was used to make the linkage between components, such as wing and tail. A description of the input parameters for each component of the aircraft is shown in following paragraph

Wing

At this stage, no airfoil had been chosen, which was not a problem because the model from [45] can be used by imputing parameters from airfoil characteristics and design, such as thickness-to-chord ratio and location of maximum thickness. Choosing an airfoil in such an early stage would mean to prescribe the wing thickness-to-chord ratio, which could result in a non-optimum solution. This approach allowed the optimizer to compute the best wing dimensions without major constraints. Nowadays, there are several projects that couple airfoil with wing optimization, allowing to obtain a custom fully optimized wing, for a specific operation [52] [53]. However, it was not possible to develop those capabilities on the optimizer, wherefore some parameters were prescribed, based on nowadays practices, for model simplification:

$x/c_{t_{max}}$ maximum thickness position, set at 30% of chord length, based on typical 4 and 5-digit NACA airfoils [54]

e Oswald Coefficient kept equal to 0.8 for simplicity;

λ Taper ratio of 0.8, to approximate the lift distribution to an ellipse [45]

All remaining parameters regarding the wing were defined accordingly to the project requirements.

Fuselage

The aerodynamic model discussed on Chapter 3 was the same used during the optimization

Wing tip Pod

Assuming the pods could be treated as a blended body, the Sears-Haack approach for the fuselage was used to estimate the pods' parasite drag, with parameters defined in Table 4.1. Due to its location at the wing tips, the interference factor Q was defined as 1.25 [45].

Parameter	Value
Length $[m]$	0.42
Maximum Diameter $[m]$	0.16
Fineness Ratio	0.38
Mass $[kg]$	0.25

Table 4.1: Wing Tip pod parameters

Tail

Due to modifications on the wing, it was necessary to account for changes in the tail geometry. These were estimated using Corke's approach on aircraft design process [45]:

- Horizontal Tail

  The expression used to calculate the area of the horizontal tail is presented below:

  $$S_{HT} = c_{HT}\frac{\bar{c}_w Sw}{l_{HT}} \tag{4.8}$$

  Where c_{HT} is the horizontal tail coefficient. Due to the dimensions and configuration, the N1 was approximated to a sail plane, to which $c_{HT} = 0.5$; l_{HT} is the distance between the aerodynamic centres of wing and horizontal, which is 1.4m, assuming no changes in the fuselage; $\bar{c}_w$ is the wing mean chord and S_w is the wing area;

- Vertical Tail

  To calculate the vertical tail area, the following equation was used:

  $$S_{VT} = c_{VT}\frac{b_w Sw}{l_{VT}} \tag{4.9}$$

  Where c_{VT} is the vertical tail coefficient (c_{VT} =0.02), and l_{VT} is the distance between the aerodynamic centres of wing and horizontal, which is 1.3m, assuming no changes in the fuselage;

To keep the similarity to the N1, all remaining parameters from tables 3.3 and 3.4 were kept the same.

4.1.2 Parametric Study

With all variables and models defined, it possible to summarize the problem in terms of optimization notation.

$$\begin{aligned}
\text{minimize} \quad & W_{fuel} \\
\text{by varying} \quad & t_{wing}, S_{wing}, b_{wing} \\
\text{subject to} \quad & t_{wing} \geq 0.035 \\
& S_{wing} \geq 1.08 \\
& 2.3 \leq b_{wing}/2 \leq 2.45 \\
& (t/c)_{wing} = constant \\
& L = W \\
& V_{cr} = 50 \\
& V_{ltr} = 40
\end{aligned}$$

Initially, the objective was set to minimize the aircraft drag, D. However, due to the existence of various segment, which have different parameters and requirements, it was noted that the value for the minimum drag is not always coincident. In other words, the inputs that minimize the drag during the cruise stage may differ from the ones that minimize the patrol stage. Since the final objective is to obtain a fixed-wing aircraft, the solution must fit both stages.

Therefore, considering that, in steady, horizontal flight, $T = D$ and knowing T varies with the aircraft's fuel consumption, by minimizing the total amount of fuel for the mission, the configuration that suits best for both segments is achieved. When optimizing an aircraft for cruise, designers typically look to minimize its drag [44], so the aerodynamic efficiency is as high as possible. When the goal is to optimize the loiter stage, the parameter of minimization is the flight power required [44], which is given by:

$$P_{req} = T \times V_{stage} \tag{4.10}$$

In this case, because V_{stage} is defined as constant, the minimization can be done by just looking for minimum drag during loiter.

The diagram in Figure 4.4 helps to visualize how the optimizer works.

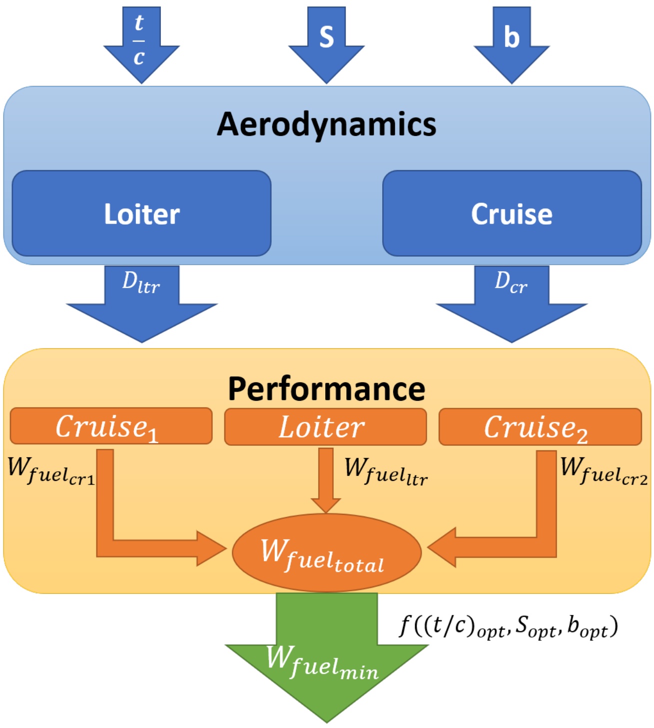

Figure 4.4: Optimization Chart

The design variables thickness, wing area and wing span are defined in a vector form $\vec{v}$, presented in the following form:

$$\vec{v} = (x_1, x_2, ..., x_m) \tag{4.11}$$

where x_m corresponds to each scalar independent variable.

The aerodynamic model computes the aircraft's drag, accounting for the wing tip pods, for each combination of inputs, for each flight segment: cruise to target area, loiter and returning cruise. The computation returns an array of $j \times k$ matrices, which are the entries of a $1 \times i$ vector:

$$\vec{D} = \begin{bmatrix} \begin{bmatrix} D_{11} & \cdots & D_{1k} \\ \vdots & \ddots & \vdots \\ D_{j1} & \cdots & D_{jk} \end{bmatrix}_1 & \begin{bmatrix} D_{11} & \cdots & D_{1k} \\ \vdots & \ddots & \vdots \\ D_{j1} & \cdots & D_{jk} \end{bmatrix}_2 & \cdots & \begin{bmatrix} D_{11} & \cdots & D_{1k} \\ \vdots & \ddots & \vdots \\ D_{j1} & \cdots & D_{jk} \end{bmatrix}_i \end{bmatrix}$$

Simplifying in terms of mathematical notation, the process is defined as

$$\left[\left(D_{ijk}\right)_{cr1} \left(D_{ijk}\right)_{ltr} \left(D_{ijk}\right)_{cr2} \right] = f\left(\left(t/c\right)_i, S_j, b_k \right) \tag{4.12}$$

To guarantee that thickness at the wing root met the requirements, it was necessary to create a verification step, prior to the computation. The mean aerodynamic chord $\bar{c}$ can be computed from the wing area S and the wing span b, using the following equation [45]:

$$\bar{c}_{(u,v)} = \frac{S_u}{b_v} \tag{4.13}$$

where S_u and b_v are scalar entries from $\vec{S}$ and $\vec{b}$.

Next, rearranging Equation (4.36) from Corke [45], the tip chord can be computed using the following equation:

$$c_{tip_{(u,v)}} = \left(\frac{3 \times \bar{c}_{(u,v)} \times \lambda}{2} \right) \left(\frac{1+\lambda}{1+\lambda+\lambda^2} \right) \tag{4.14}$$

where λ is the taper ratio of the wing.

Then, since the wing was defined with a fixed thickness-to-chord ratio, the thickness at the tip was given by

$$t_{tip_{(w,u,v)}} = \left({}^{t}/{}_{c}\right)_w \times c_{tip_{(u,v)}} \tag{4.15}$$

where $\left({}^{t}/{}_{c}\right)_w$ is a scalar entry from $\vec{t/c}$.

Finally, a checkpoint is reached: if $t_{tip_{(w,u,v)}} \geq 0.035(m)$, the script starts the optimization, if $t_{tip_{(w,u,v)}} < 0.035(m)$, the final solution is not inside the feasible region, so the script disregards variables $\left(\left({}^{t}/{}_{c}\right)_w, S_u, b_v\right)$ and advances to next set of input variables.

This avoids the computation of inconvenient configurations and the total drag D_{ijk} of each segment is computed for the variables that guarantee the requirements are fulfilled.

Then, the total mass fuel is computed from each entry D_{ijk}

$$P_{shaft} = \frac{T \times V_{stage}}{\eta_{prop}} \tag{4.16}$$

From horizontal flight equations, $T = D$, which means

$$P_{shaft_{ijk}} = \frac{D_{ijk} \times V_{stage}}{\eta_{prop}} \tag{4.17}$$

Additionally, it is necessary to account for 150W to supply electric energy to avionics.

From the engine's datasheet, is possible to know its specific fuel consumption: $C = 0.432[kg/kW.h]$.

Finally, the mass of fuel can be calculated putting all these parameters in the following equation

$$m_{fuel_{ijk}} = C \times \left(\frac{P_{shaft_{ijk}}}{1000} \times \Delta t_{stage} \right) \tag{4.18}$$

where $P_{shaft_{ijk}}$ is in Watts, W, and the Δt_{stage} in hours, h.

For the cruise segment, Δt_{stage} can be computed using motion equation and knowing the range and speed required for this stage,

$$\Delta t_{cr} = \frac{R \times 3600}{V_{cr}} \tag{4.19}$$

so Δt_{cr} is expressed in hours.

For the search segment, $\Delta t_{ltr} = E$.

In the end, the mass of fuel consumed is summed, considering losses and fuel reserve, similar to Chapter 3

$$M_{ijk} = \left[\left(m_{fuel_{ijk}} \right)_{cr1} + \left(m_{fuel_{ijk}} \right)_{ltr} + \left(m_{fuel_{ijk}} \right)_{cr2} \right] \times 1.06 \tag{4.20}$$

where M_{ijk} is the total fuel mass.

This computation allows to obtain the configuration that requires the least amount of fuel to carry the required operation, which can be considered as the most aerodynamically effective, once it minimizes the overall drag of the aircraft.

$$M_{min} = f\left(t_{opt}, S_{opt}, b_{opt}\right) \tag{4.21}$$

4.2 Result Discussion

4.2.1 Optimizer Output

Consider the following table:

Input vectors	**Values**
Thickness-to-chord ratio $\vec{t/c}$	$[0.13 : 0.01 : 0.20]$
Wing Area $\vec{b}$	$[1.08 : 0.01 : 1.5]$
Wing Span $\vec{S}$	$[4.6 : 0.01 : 4.9]$

Table 4.2: Input Variables

The input vectors are described in the following notation: $\vec{v} = [A : j : B]$, where $\vec{v}$ is an example vector, A is the minimum value, B the maximum and j the step, which, in another notation, means

$$[A:j:B] = \left[A,\ (A+j)\,,\ (A+2j)\,,\ (A+3j)\,, ...B\right]$$

Decreasing the value of j will increase the size of $\vec{v}$, which is the number of scalar variables to process, which is computed as follows

$$size(\vec{v}) = 1 + \frac{B-A}{j} \tag{4.22}$$

Knowing that each scalar is processed individually, large input vectors means longer computation time. However, some optimizing functions can be sensitive to input variables, giving approximate values of the optimum minimum instead. A trade-off between result accuracy and computation effort must be considered in this cases. The step j has a crucial consequence on this matter, as it allows to define the level of accuracy and effort the optimizer it have. It comes to the user to define this parameter. In this case, a step $j = 0.01$ for all design variables is sufficient to allow the optimizer to return accurate results with low computation time.

Returning to input variables in Table 4.2, although only the wing span had boundaries for the maximum and minimum values, the remaining two parameters had to have a limit for the maximum value. This happened due to limitations in the MATLAB script and requires adjustments in their values if returned as optimal solutions.

After processing, for a search time of 8 hours, the output is the following:

Parameter	**Value**
Wing Area m^2	1.08
Wing Span m	4.67
$\overline{c}\ m$	0.231
Root Chord m	0.256
Thickness at Wing root m	0.044
Tip Chord m	0.205
Thickness at Wing tip m	0.035
Thickness-to-chord ratio	0.171
Aspect Ratio	20.2
Total Fuel Mass kg	8.71

Table 4.3: Wing Dimensions

From Table 4.3, it is possible to notice that the optimum values for the wing area and wing tip's thickness are minimum in the respective design variables' vector. Re-running the MATLAB script with different inputs resulted into smaller values for the fuel consumed, but the solution would be outside the feasible area and so it was disregarded. Another aspect is that none of optimum solution correspond to the maximum value of the design variables, in the case of the wing span b and thickness-to-chord ratio t/c. This means the final solution is the optimal for the limits imposed to the solver.

4.2.2 Post-Processing

Before starting the discussion on the results, it is important to highlight this study **did not account** for the VTOL system, since complex aerodynamic phenomena would occur on that location on the wing. That evaluation requires the use of wind-tunnel testing or Computational Fluid Dynamics (CFD) to accurately characterize the generation of lift and drag of the fully equipped wing.

Aerodynamics

The analysis also allows to assess the impact of flying with the wing tip pods, since both configurations, with and without them, are evaluated.

Segment	Pods Unmounted	Pods Mounted
Dash to Target Area	0.012	0.018
Search/Patrol	0.013	0.018
Dash to Home Point	0.012	0.018

Table 4.4: Wing tip pod influence in the aircraft C_{D_0} at each segment

Segment	C_L
Dash to Target Area	0.208
Search/Patrol	0.301
Dash to Home Point	0.175

Table 4.5: Lift coefficient C_L from the optimizer

The addition of the pods at the wing tips have strong influence on the aircraft's parasite drag, increasing its value in approximately 45% for all segments. The additional drag has a major consequence on fuel consumption, which, when recomputing the fuel for the initial configuration with the process on Chapter 3, increases from 5.24kg to 7.23kg.

From Table 4.3, the fuel mass consumed for the optimal configuration is 8.71kg, which means an increase of 17%kg on the fuel consumption, between the initial configuration and the optimized one, when the pods are accounted. This is mainly due to the difference between the thickness-to-chord ratios for both configurations, that caused an increase of approximately 19% on wing's Form Factor, $\mathcal{F}$, and, consequently, on the wing's parasite drag. This component is the main responsible for the increase on the fuel consumption, since there is an overall reduction of approximately 70% on the induced drag. The reason behind this fact are the increase of the wing's aspect ratio, from 14.75 to 20.2, and the reduction of the lift coefficient, C_L, due to the increase on the wing area.

The values for the lift and drag coefficients for the configuration without pods are similar to the ones computes in Chapter 3. This is mainly due to the similarity on the planform area between the optimized and reference wing.

In terms of manufacturing, this solution is very positive for the project and the aircraft because it is possible to assume the mass of the wing will not change, since, when using composite materials and keeping a similar thickness of skin, it is legit to assume $m_{wing} \propto S_{wing}$ [34]. However, a detailed study on the minimum thickness and total volume of composite materials required to manufacture this structure should be performed, to accurately compute the optimized wing's mass.

Analysing now the lift-to-drag on Table 4.6, the same situation verifies. In qualitative terms, this solution is possibly one of the best to fit the problem, because the new configuration demonstrates similar aerodynamic characteristics to an airplane well-known from designing time.

Segment	Pods Unmounted	Pods Mounted
Dash to Target Area	15.73	10.97
Search/Patrol	20.49	14.85
Dash to Home Point	13.57	9.37

Table 4.6: Comparison for the wing tip pod influence in the aircraft L/D at each segment

Lastly, the L/D ratio also suffers a large decrease when wig tip pods are installed in the aircraft. With an average cut of 42% in the cruise stages and 36% on the patrol, it is possible to conclude they highly reduce the aircraft's aerodynamics, making the third largest contribution to generation of drag, as shown in Figure 4.5.

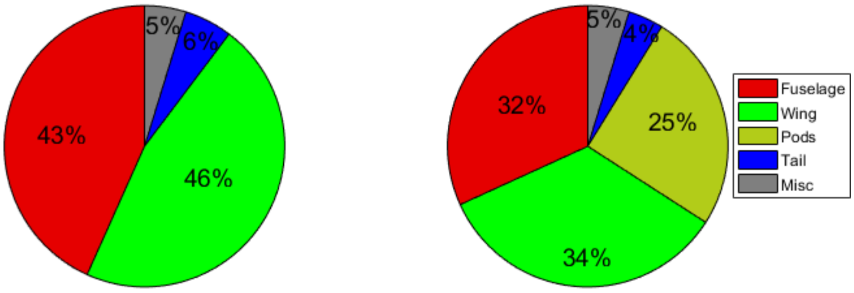

Figure 4.5: Drag sources during cruise: on the left configuration with unmounted pods; on the left the configuration with the pods mounted, generating 25% of the total aircraft drag

However, by being placed in the wing tips, there are benefits upon generation of induced-drag that were not accounted in this study, and certainly need to be assessed, given the fact that it was proven fuel consumption varies with wing tip modifications [42].

Having established the dimensions of the wing, it was necessary to compute its $\frac{dC_L}{d\alpha}$ slope, an aerodynamic parameter that allows the computation of the wing's lift coefficient C_L[5] as function of α.

For subsonic flight, the value of $\frac{dC_L}{d\alpha}$ can be computed using the following expression [45]

$$C_{L_\alpha} = \frac{C_{l_\alpha} AR}{2 + \sqrt{4 + (AR\beta)^2 \left(1 + \frac{\tan^2\left(\Lambda_{t/c}\right)}{\beta^2}\right)}} \tag{4.23}$$

where $\beta = \sqrt{1 - M_{eff}^2} = \sqrt{1 - M_\infty^2}$. Computing β for both cruise and loiter segments, is obtained $\beta_{cr} = 0.989$ and $\beta_{ltr} = 0.993$, which means $\beta \approx 0.99$. As highlighted before, the sweep angle is considered null over the wing, so the value of $\tan^2\left(\Lambda_{t/c}\right) = 0$ in Equation (4.23).

Typically, it is computed by converting the airfoil's $\frac{dC_l}{d\alpha}$. However, since no airfoil was selected for the computation of the optimum wing dimensions, there is no information about the variation of the lift

[5]Concerning aerodynamic coefficients: if the index is capital (C_L), is it referring to wing characteristics; if it is lower case letter (C_l), it is relative to the airfoil

coefficient C_l with α. Therefore, it is assumed as initial computation the lift-slope $\frac{dC_l}{d\alpha}$ to be equal to 2π [45]. Therefore,

$$C_{L_\alpha} = \frac{2\pi AR}{2 + \sqrt{4 + (AR\beta)^2}} = 5.74 rad^{-1} \tag{4.24}$$

Magnetics

When computing the magnetic interference at the optimum wing span, $b_{opt} = 4.67m$, the value from the approximation function defined on Equation (4.2) returns $\beta_{wingtip} = -1.88$nT. This value is not a surprised because any value of $b > 4.6$m would give a value smaller than 2nT for the magnetic noise, due to the feasible region established in the beginning. However this only the approximation of a theoretical model. To prove the reliability of this result, a computational analysis was carried using a *COMSOL* magnetic model of the airplane, defined by Hansen [8]

This finite-element software requires the definition of the environmental conditions and all components of the aircraft, inside a finite computational domain [8]. After setting all the parameters, it runs the computation over the domain, measuring the parameter of interest, which in this case, was the intensity of the magnetic inside a defined volume. To analyse a particular coordinate, *COMSOL* allows to load the overall analysis and uses "probes" to scan a specified area. In this case, these "probes" were used at both wing tips, $y = \pm 2.335$ which provided different results: the left wing tip measurement was $\beta = -2.27$nT and the right wing tip was 2.04nT. This results are concordant with magnetic model explained in Chapter 3.

The error between the theoretical and the computational was computed using the following expression

$$\varepsilon = \frac{b_{comp} - B_{theo}}{B_{theo}} \approx 9\% \tag{4.25}$$

The value of the error between analysis was in the same magnitude as the errors registered by Hansen in its study [8], so the result was considered valid and successful, although the computational result is slightly higher than the requirements. In general, the final results represent a decrease of the magnetic noise at the wing tip of approximately 30% for the computational analysis and 35% in the theoretical.

In Figure 4.6, is possible to see the aircraft during a *COMSOL* analysis.

As a final remark, since all constraints were satisfied, it is possible to conclude the optimization process was a success.

4.2.3 Structures

During flight, there are load limits the aircraft must not surpass to keep its structural integrity. The V-n diagram establishes the flight load factors that are used for the structural design as a function of the

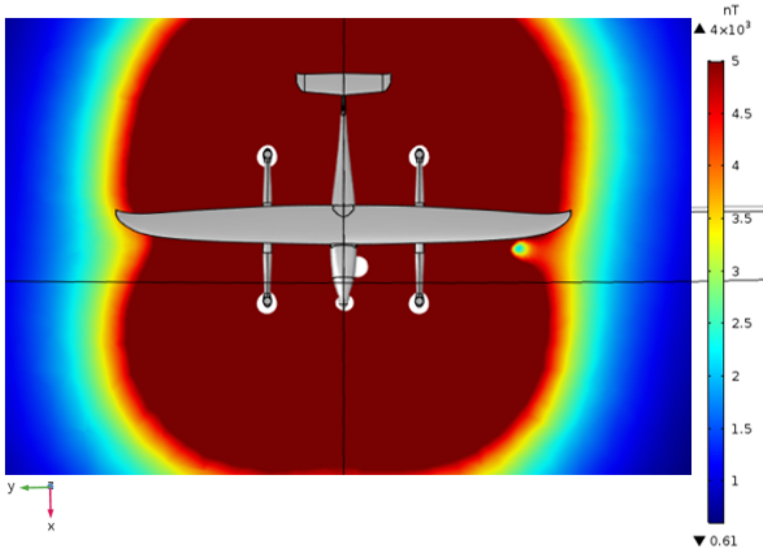

Figure 4.6: *COMSOL* output calculations

air speed. These load factors, defined as $n = L/W$, are the maximum loads the aircraft will experience and are referred to as the *limit load factors*.

Based on FAR-23, from table 10.1 from [45], for a normal Sailplane aircraft the load factor interval is $-1 \leq n \leq 3$.

The V-n diagram should be designed for every flight altitude, but it will only be considered in cruise, because of the mission profile.

The V-n diagram designed, in cruise conditions, is presented in Figure 4.7.

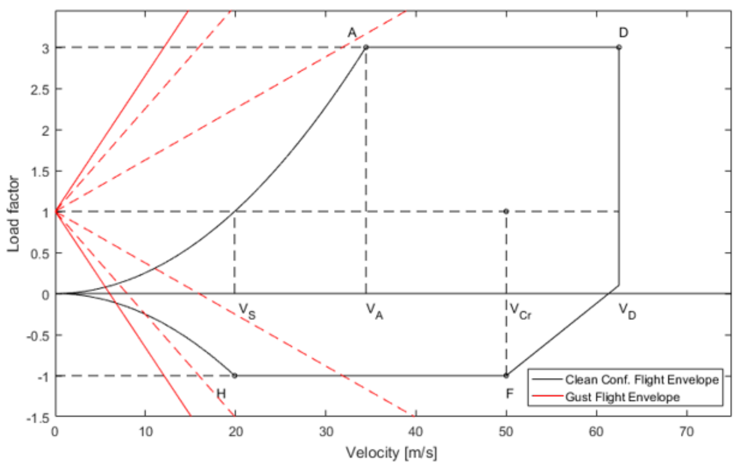

Figure 4.7: V-n Diagram for cruise

The curve from $n = 0$ to A represents the maximum load produced by high angle of attack. That curve and the curve from $n = 0$ to H are given by:

$$n = \frac{\frac{1}{2}\rho V^2 C_{L_{max}}}{W/S} \tag{4.26}$$

The maximum and minimum values at A and H are defined by the FAR standard for this type of aircraft. At point A the corresponding velocity is $V_A = 35.5m/s$.

V_c represents the cruise speed, at $n = 1$, when lift equals weight.

Point D occurs at dive speed, that is the highest velocity during flight.

$$V_D = 1.5V_C \tag{4.27}$$

Lines $A-D$ and $H-F$ represent the largest positive load factor and negative load factor, respectively.

The intersection of the line $n = 1$ with the curve $0 - A$ corresponds to the stall velocity, that is the minimum speed at which the aircraft can maintain level flight. This speed is $V_S = 22m/s$

Point F is the intersection between the negative load limit and the cruise speed V_C and connects the negative load limit with the dive speed V_D and closes the flight envelope.

The V-n diagram must also take into account the load factor due to gusts. Gust loads are unsteady aerodynamic loads produced by atmospheric turbulence and they represent a load factor that is added to the aerodynamic loads.

The incremental load factor due to gusts is:

$$\Delta n = \frac{\rho u V C_{L_\alpha}}{2W/S} \tag{4.28}$$

The gust load factor is then, for cruise ($n = 1$):

$$n = 1 + \Delta n \tag{4.29}$$

The normal component of the gust velocity is the product of the statistical average of values taken from flight data $\hat{u}$ and the response coefficient K:

$$u = K\hat{u} \tag{4.30}$$

According to [45] (table 10.3), the statistical values for gust velocities for different flight conditions, for an altitude range from 0 to $20000ft$, where the cruise altitude of our aircraft fits in, are:

1. High angle of attack: $\hat{u} = 66ft/s$
2. Level flight: $\hat{u} = 50ft/s$
3. Dive Condition: $\hat{u} = 25ft/s$

The response coefficient for subsonic flight is given by:

$$K = \frac{0.88\mu}{5.3 + \mu} \tag{4.31}$$

The mass coefficient μ, that affects the frequency response of the aircraft to turbulence, is defined by:

$$\mu = \frac{2W/S}{\rho g \bar{c} C_{L_\alpha}} \tag{4.32}$$

Because the mass of the aircraft is small (MTOW – 35 kg), the standard gust values of 25, 50 and 66 [ft. /s] or 7.62, 15.24, 20.12 [m/s] result in large values of load factor that greatly surpass the maneuvre envelope and, therefore, do not allow for a typical combination of both diagrams.

4.2.4 Mass Breakdown

The last step of this study is the verification of the mass of all components installed in the aircraft. So far, the total mass is given by

$$m_{UAV} = m_{airframe} + m_{MAD-XR} + m_{CW} + m_{fuel} \tag{4.33}$$

The airframe on combustion configuration has mass of 17.7kg, the MAD-XR is composed by two components that weigh 2.5kg together accounting the wiring, the CW'mass is equal to the MSU's and the fuel 8.71kg, making a total 32.67kg.

This means the VTOL system, in order to the aircraft do not exceed 35kg in the final configuration, can not be heavier than 2.33kg.

By the time the project was conducted, the N1's VTOL system did not existed, although the aircraft was designed to be accounting with that capability. Therefore, a study on the VTOL system was carried, to design a MATLAB quadcopter model that computes the power required for the aircraft on take-off and landing. This model can later be used when more specific details about the aircraft operation are available.

VTOL

As described earlier, the VTOL systems has 4 electric propeller motors. Their mission is provide enough thrust T that allows the aircraft to take-off and safely land.

In both cases, at some point, the aircraft will be hovering above ground, even if it for a very short period of time, when making the transition between vertical and horizontal flight, and vice-versa. On helicopter performance, computing the power to hover is required as it is a reference value for the computations of vertical flight [55].

The power to hover can be computed using Rankine's disk actuator theory. The rotor is modelled as an infinitely thin disc, inducing a constant velocity along the axis of rotation [55].

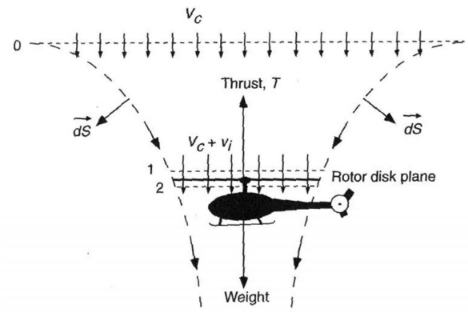

Figure 4.8: Representation o disk actuator theory on helicopter [55]

In hover, the velocity represented by V_C in Figure 4.8 is null, since it is assumed there is no axial motion [55].

The thrust generated by the disk can be computed using the following equation

$$T = 2\rho A {v_r}^2 \tag{4.34}$$

where v_r is the induced velocity at the disk plane and A is the disk area. In hovering case, v_c is denoted as v_h.

The ideal power to hover is given by

$$P = T v_h \tag{4.35}$$

Rearranging Equation (4.34), the common formulation for the power expression is given by

$$P = T\sqrt{\frac{T}{2\rho A}} = \frac{T^{3/2}}{\sqrt{2\rho A}} \tag{4.36}$$

Upon preliminary helicopter design, it is necessary to account for non-ideal physical effects, such as tip losses or finite number of blades. Therefore, an empirical correlation factor called *induced factor* k, is added to the equation [55]

$$P = k\frac{T^{3/2}}{\sqrt{2\rho A}} \tag{4.37}$$

Typically, $k = 1.15$.

In order for an helicopter to hover, the thrust generated by the rotor must equal the aircraft's weight, $T = W$. In this project case, there are four rotors and is made the assumption that the amount of thrust generated by each of them is the same and is equal to one-quarter the aircraft's weight.

From the experience of the personnel from UVic CfAR, electric motors typically generate heat when in operation, which is increased if working in a regime of maximum power. To avoid a motor to become inoperative and to guarantee the aircraft has a margin for manoeuvrability, is it necessary to account for a safety factor, SF, for the thrust-to-weight ratio T/W, typically higher than 1.3.

$$T_{rotor} = SF\frac{1}{4}W \tag{4.38}$$

From Equation (4.37) is possible to note the power is inversely proportional to the $\sqrt{A}$. An increase of the propeller diameter will reduce the power required but will also increase the total added mass by a factor of 4, since this is the number of motors.

Finally, it is necessary to losses during this process. Neither the propeller, motor or electrical system are fully efficient, which means it is necessary to supply more power than the actual motor output, required to hover. From experience, a propulsive efficiency of 85% was accounted for the computation.

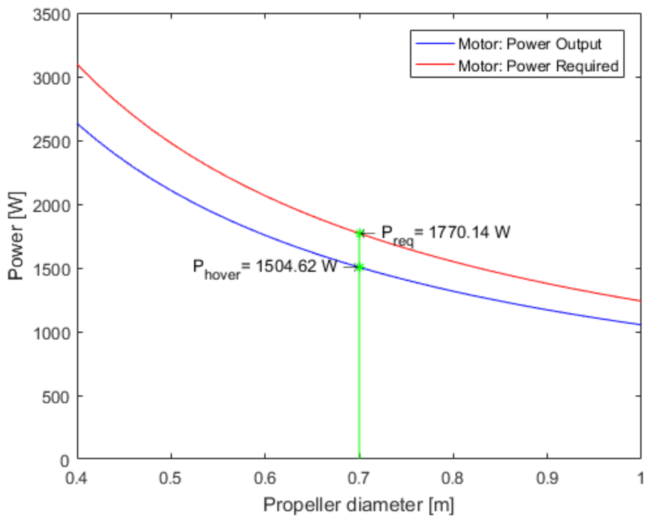

Figure 4.9: Determination of the output power of each motor along with the power supplied

Figure 4.9 shows the variation of the output and required power with propeller diameter for the specified T/W for each motor, using a safety factor of 1.5 and propellers with 0.7m of diameter.

This model allows an accurate estimation of the power required for the VTOL stages, which along the mass availability, can be used to find the best combination of motors and batteries that suits the target operation.

Analysing typical suppliers and products for electric drones, it was simple to conclude that was not going to be possible to install a VTOL system for the N1, within the mass limitations.

5

Conclusions and Future Work

Contents

5.1 Conclusions

The thesis is included in a project that intends to develop a UAV, capable of conduct independent MAD missions, in search of submerged metallic vehicles, while performing VTOL from a ship. With the rising capabilities of submarines to evade sonar, MAD sensors have become valuable tools on detection and identification. Starting with a pre-existing aircraft, the NEBULA N1, it was studied the best to way instrument the MAD sensor, whilst enhancing its performance and meeting the operational requirements. The final goal was to obtain an hybrid aircraft, that performs VTOL with electric motors, and patrol and dash segments with a combustion engine, since it is required to execute search flight of 8 hours at 40m/s, after a 20nm dash at 50m/s.

When performing a magnetic survey, it is crucial to guarantee that the magnetometer is free from any magnetic noise source and that its data is accurately scaled and accounts for external interference. This does not disregards the fact that magnetic clearance is required.

Therefore, based on the magnetic characterization of the aircraft, two solutions were considered: to place the sensor at the wing tip, where the aircraft's magnetic field is the weakest, or design a tail stinger boom, long enough to match the measurements at the wing tip. The criteria of choice were the amount of mass that each configuration required to keep the aircraft stable and the time required to modify the airframe, due to the project schedule. In the end, with an initial estimate of 2kg for the MSU container and harnessing, the wing tip was the option that required the lightest counterweight, saving up to 5kg of payload when compared to the tail configuration. This solution, however, had a drawback. Due to the MAD-XR specifications, the cabling that connects the MSU and the interface unit has components that are larger than the wing thickness, requiring special mounting and maintenance actions, which could compromise the sensor well-functioning. Also, despite the wing tip's relatively low magnetic signature, it was suggest to find a solution that could decrease its intensity. These requirements were considered alongside with the required operational performance. Then, it was decided to conceptualize a modification on the N1's wing, to obtain the optimal solution that meets the specification from all the parties involved the project.

An aerodynamic characterization of the N1 was carried, based on aircraft design theory and local collected data, from flight testing experience and measurements on the aircraft. The model showed an error of 5.8% when compared to the experimental results, proving it could be used on the optimization for the new wing sizing. A survey on N1 performance was carried for the required mission profile, which includes a 20nm dash at 50 m/s, a 8-hour search segment over a target area and a return dash in the same conditions as the first. The results showed a fuel consumption of 7.23kg, considering the aerodynamic effects of the wing tip pods, where the MAD sensor is harnessed.

At this point, an optimization process was conduct, with the objective of minimize the fuel consumption. The design variables were the wing thickness-to-chord ratio, area and span, and the constraints were dictated from the magnetic, operational and aerodynamic disciplines involved in the process. To guarantee a feasible solution, a parametric optimization was used, where the total fuel consumption was computed for every combination of input variables. This resulted in a minimum value of 8.71kg for the mission listed above, accounting for the wing tip pods. Furthermore, the optimization method ensured that all constraints were satisfied during the process, obtaining a configuration that suits the project requirements.

This configuration dictated an increment of 20% in the aircraft wing span, slightly increasing the wing area, which gave the aircraft a similar aerodynamic efficiency when compared to the initial reference. The major accomplishment of the optimizer is a decrease of 30% in the magnetic noise, measured at new sensor's location, which decreases the chances of obtaining unreliable analysis. However, dimensional requirements, such as the MAD sensor's wiring accommodation, caused an increase in the wing thickness.

5.2 System Limitations and Future Work

As highlighted during the report, this was a conceptual study for a wing modification. It is based on several theoretical assumptions, commonly used on aircraft design processes, which may return results with a low level of precision, when compared to flight data of a fully designed airplane. Also, the fact the optimizer does not require a specified airfoil as an input, may be a benefit for future analysis. Due to the lack of time, it was not possible to conduct a detailed research on airfoils and airfoil optimization, which is an area of growing interest in the last years.

It is also recommended a detailed analysis, using CFD, on the wing aerodynamics when the VTOL system is installed, to improve the results obtained in this work, and structural analysis of the aircraft, especially on the wing, due to the amount of system attached to it.

It would also be pertinent to conduct a new equilibrium analysis for a gas propulsion configuration, after verifying the position of each system in the airframe. In this regard, flight testing should be conduct, to study the aircraft performance on this configuration and verify the model developed on this project.

Additionally, it may beneficial to study how to distribute the batteries that provide energy to VTOL engines. Since there are four, placing a smaller battery on every VTOL nacelle, in such way that they cancel the moment each other, should be considered, if there is no room for a large battery in the fuselage. This configuration would also reduce the wiring's weight.

Finally, and taking into account all the results obtained, it is recommended to study the possibility of acquiring and design a new aircraft for the proposed operation, since the N1 does not fit all the specifications and requires several modifications.

Bibliography

[1] I. Serrano, "Unmanned aircraft system (uas) vs. manned aircraft system (mas): A military aircraft study," 2015. [Online]. Available: http://digitalcommons.lmu.edu/etd/430

[2] "Total submarine strength by country," Global Fire Power, [Accessed in 1-10-18]. [Online]. Available: https://www.globalfirepower.com/navy-submarines.asp

[3] S. Tumanski, *Handbook of magnetic measurements*. CRC press, 2016.

[4] F. T. Ulaby, E. Michielssen, and U. Ravaioli, *Fundamentals of Applied Electromagnetics 6e*. Prentice Hall, 2001.

[5] D. Jiles, *Introduction to magnetism and magnetic materials*. CRC press, 2015.

[6] T. V. WILSON, "How magnets work," How Stuff Works?, [Accessed in 1-10-18]. [Online]. Available: https://science.howstuffworks.com/magnet4.htm

[7] N. A. Spaldin, *Magnetic materials: fundamentals and applications*. Cambridge University Press, 2010.

[8] C. Hansen, "Magnetic Signature Characterization of a Fixed-Wing Vertical Take-off and Landing (VTOL) Unmanned Aircraft Vehicle (UAV)," Master's Thesis, University of Victoria, 2018.

[9] B. Parker, "Geomagnetism - Class Notes 1," Institute of Geophysics and Planetary Physics, University of California, 2013. [Online]. Available: https://igppweb.ucsd.edu/parker/SIO229/geomag01-14.pdf

[10] M. N. Nabighian, V. Grauch, R. Hansen, T. LaFehr, Y. Li, J. Peirce, J. Phillips, and M. Ruder, "The historical development of the magnetic method in exploration," *Geophysics*, vol. 70, no. 6, pp. 33ND–61ND, 2005.

[11] D. Kumar and D. Kumar, "Chapter 3 - evaluation of coking coal resources and reserves," in *Management of Coking Coal Resources*, D. Kumar and D. Kumar, Eds. Elsevier, 2016, pp. 61 – 112. [Online]. Available: http://www.sciencedirect.com/science/article/pii/B9780128031605000034

[12] A. Sheinker, L. Frumkis, B. Ginzburg, N. Salomonski, and B.-Z. Kaplan, “Magnetic anomaly detection using a three-axis magnetometer,” *IEEE Transactions on Magnetics*, vol. 45, no. 1, pp. 160–167, 2009.

[13] A. Sheinker and M. B. Moldwin, “Magnetic anomaly detection (mad) of ferromagnetic pipelines using principal component analysis (pca),” *Measurement Science and Technology*, vol. 27, no. 4, p. 045104, 2016.

[14] CAE, “Magnetic Anomaly Detection Extended Role (MAD-XR),” Product Datasheet, 2018. [Online]. Available: https://www.cae.com/defence-security/operational-systems/magnetic-anomaly-detection-extended-role-mad-xr/

[15] United States Navy, “UNDERWATER DETECTION AND TRACKING SYSTEMS,” Fundamentals of Naval Weapons Systems, [Accessed in 04-09-18]. [Online]. Available: https://fas.org/man/dod-101/navy/docs/fun/part09.htm

[16] Y. Ege, A. Kakilli, O. Kılıç, H. Çalık, H. Çıtak, S. Nazlıbilek, and O. Kalender, “Performance analysis of techniques used for determining land mines,” p. 1163, 2014.

[17] MarineBio Conservation Society, “Submarines and Deep Technology - MarineBio.org,” 2014, [Accessed in 04-09-18]. [Online]. Available: http://marinebio.org/oceans/submarines/

[18] R. Hill, *Anti-Submarine Warfare*, 2nd ed. Annapolis: Naval Institute Press, 1989.

[19] A. Other and N. Webmaster, “Anti-Submarine Measures from World War I,” 2005, [Accessed in 04-09-18]. [Online]. Available: https://www.navyhistory.org.au/anti-submarine-measures-from-world-war-i/

[20] “Sinking Of The Linda Blanche Out Of Liverpool,” Fine Art America, [Accessed in 06-09-18]. [Online]. Available: https://fineartamerica.com/featured/sinking-of-the-linda-blanche-out-of-liverpool-willy-stoewer.html

[21] B. Drinkwater, “How to find a submarine (no, it’s not just a case of flicking the sonar on),” 2014, [Accessed in 14-09-18]. [Online]. Available: https://theconversation.com/how-to-find-a-submarine-no-its-not-just-a-case-of-flicking-the-sonar-on-33343

[22] T. Video, “How do submarines stay undetected?” 2014. [Online]. Available: https://www.telegraph.co.uk/news/worldnews/europe/sweden/11181064/How-do-submarines-stay-undetected.html

[23] “Air anti-submarine warfare,” GlobalSecurity.org, [Accessed in 04-09-18]. [Online]. Available: https://www.globalsecurity.org/military/systems/aircraft/asw.htm

[24] J. R. Reynolds, “Submarines, sonar, and the death of whales: Enforcing the delicate balance of environmental compliance and national security in military training,” *Wm. & Mary Envtl. L. & Pol’y Rev.*, vol. 32, p. 759, 2007.

[25] L. Brekhovskikh and Y. Lysanov, *Fundamentals of Ocean Acoustics*, ser. Springer Series on Wave Phenomena. Springer Berlin Heidelberg, 2013. [Online]. Available: https://books.google.pt/books?id=AVfuCAAAQBAJ

[26] R. A. Frosch, “Underwater sound: Deep-ocean propagation: Variations of temperature and pressure have great influence on the propagation of sound in the ocean.” *Science*, vol. 146, no. 3646, pp. 889–894, 1964.

[27] V. A. Kaharl, “Sounding Out the Ocean’s Secrets,” 1999, [Accessed in 14-09-18]. [Online]. Available: http://www.nasonline.org/publications/beyond-discovery/sounding-out-oceans-secrets.pdf

[28] B. H. Maranda, *Passive Sonar*. New York, NY: Springer New York, 2008, pp. 1757–1781. [Online]. Available: https://doi.org/10.1007/978-0-387-30441-0_97

[29] “Importance of ASW Helicopters for the Philippine Navy... Why block their acquisition?” MAXDEFENSE PHILIPPINES, [Accessed in 14-09-18]. [Online]. Available: http://maxdefense.blogspot.com/2014/03/importance-of-asw-helicopters-for.html

[30] Wikipedia, “Lockheed p-3 orion,” Wikipedia, The Free Encyclopedia, 2018, [Assessed in 14-09-18]. [Online]. Available: https://en.wikipedia.org/w/index.php?title=Lockheed_P-3_Orion&oldid=859199009

[31] “P-3,” GlobalSecurity.org, [Accessed in 04-09-18]. [Online]. Available: https://www.globalsecurity.org/military/systems/aircraft/p-3-specs.htm

[32] University of Rhode Island, “Sonobuoys,” Discovery of Sound in the Sea, 2017, [Assessed in 14-09-18]. [Online]. Available: https://dosits.org/galleries/technology-gallery/locating-objects-by-listening-to-their-sounds/difar/

[33] R. Vieira, “Real thaw 2015 - spotters day,” PÁSSARO DE FERRO, 2015, [Assessed in 14-09-18]. [Online]. Available: http://www.passarodeferro.com/2015/03/real-thaw-2015-spotters-day-1-m1803.html

[34] Nebula Unmanned Aerial Vehicle Systems. [Online]. Available: https://www.nebula.aero/l

[35] CAE, “Advanced Integrated Magnetic Anomaly Detection System (AIMS),” Product Datasheet, 2017, [Accessed in 04-09-18]. [Online]. Available: https://www.cae.com/defence-security/operational-systems/magnetic-anomaly-detection-extended-role-mad-xr/

[36] CAE, “Sistema de detección de anomalías magnéticas mad-xr con funciones ampliadas,” Product Datasheet, 2018, [Accessed in 04-09-18]. [Online]. Available: https://www.cae.com/defence-security/operational-systems/magnetic-anomaly-detection-extended-role-mad-xr/

[37] Brican Flight Systems Inc., “TD 100 Class II UAV – ASW CAE - Magnetic Anomaly Detection,” Product Datasheet, 2014, [Accessed in 04-09-18]. [Online]. Available: https://bricanflightsystems.ca/wp-content/uploads/2018/05/%C2%A9BFSTD100ClassIIUAVASWSubDetect.pdf

[38] G. Noriega, “Aeromagnetic compensation in gradiometry—performance, model stability, and robustness,” *IEEE Geoscience and Remote Sensing Letters*, vol. 12, no. 1, pp. 117–121, 2015.

[39] F. M. White, *Fluid Mechanics, McGraw-Hill Series in Mechanical Engineering*, 7th ed. McGraw-Hill international editions, Boston, 1998.

[40] J. D. Anderson, *Fundamentals of Aerodynamics*, 3rd ed. University of Maryland. New York, Mc Grawhill. America, 2001.

[41] T. H. G. Megson, *Aircraft Structures for Engineering Students*, 4th ed., 2007.

[42] A. F. S. Board, N. R. Council *et al.*, *Assessment of wingtip modifications to increase the fuel efficiency of air force aircraft*. National Academies Press, 2007.

[43] L. Tuck, C. Samson, J. Laliberté, M. Wells, and F. Bélanger, “Magnetic interference testing method for an electric fixed-wing unmanned aircraft system (uas),” *Journal of Unmanned Vehicle Systems*, no. 0, pp. 1–18, 2018.

[44] J. D. Anderson, *Aircraft Performance and Design*. WCB/McGraw-Hill Boston, MA, 1999, vol. 1.

[45] T. C. Corke, *Design of Aircraft*. Prentice Hall Englewood Cliffs, NJ, 2003.

[46] B. Etkin and L. D. Reid, *Dynamics of flight: stability and control*, 3rd ed. Wiley New York, 1996.

[47] L. Blain, “Minix wing tip device promises 6airliners,” New Atlas, [Accessed in 1-10-18]. [Online]. Available: https://newatlas.com/minix-wing-tip-vortex-aircraft-aerodynamics/15526/

[48] D. Raymer, *Aircraft Design: A conceptual Approach*. American Institute of Aeronautics and Astronautics, Inc., 1992.

[49] M. J. Moran, H. N. Shapiro, D. D. Boettner, and M. B. Bailey, *Fundamentals of engineering thermodynamics*. John Wiley & Sons, 2010.

[50] J. Gundlach, *Designing unmanned aircraft systems: a comprehensive approach*. American Institute of Aeronautics and Astronautics, 2012.

[51] A. Marta, *Aircraft Optimal Design - Course notes*, Instituto Superior Técnico.

[52] S. Rajagopal and R. Ganguli, “Multidisciplinary design optimization of long endurance unmanned aerial vehicle wing,” *Computer Modeling in Engineering & Sciences(CMES)*, vol. 81, no. 1, pp. 1–34, 2011.

[53] W. Jin and Y.-G. Lee, “Drag reduction design for a long-endurance electric powered uav,” *International Journal of Aeronautical and Space Sciences*, vol. 16, no. 2, pp. 311–324, 2015.

[54] M. H. Sadraey, *Aircraft design: A systems engineering approach*. John Wiley & Sons, 2012.

[55] G. J. Leishman, *Principles of Helicopter Aerodynamics*. Cambridge University Press, 2006.